

TASTE: Task-Aware Out-of-Distribution Detection via Stein Operators

Michał Kozyra¹ Gesine Reinert¹

Abstract

Out-of-distribution detection methods are often either data-centric, detecting deviations from the training input distribution irrespective of their effect on a trained model, or model-centric, relying on classifier outputs without explicit reference to data geometry. We propose TASTE (Task-Aware STEin operators): a task-aware framework based on so-called Stein operators, which allows us to link distribution shift to the input sensitivity of the model. We show that the resulting operator admits a clear geometric interpretation as a projection of distribution shift onto the sensitivity field of the model, yielding theoretical guarantees. Beyond detecting the presence of a shift, the same construction enables its localisation through a coordinate-wise decomposition, and—for image data—provides interpretable per-pixel diagnostics. Experiments on controlled Gaussian shifts, MNIST under geometric perturbations, and CIFAR-10 perturbed benchmarks demonstrate that the proposed method aligns closely with task degradation while outperforming established baselines

1. Introduction

Deep models are typically trained under the assumption that training and test samples are i.i.d. from a fixed joint distribution $P(X, Y)$. At deployment, this assumption frequently fails: the test-time marginal Q_X may differ due to changes in, for example, in sensors or preprocessing pipelines. Such shifts are commonly categorised as *covariate shift* ($Q_X \neq P_X$ with $P(Y | X)$ unchanged), *label shift* (changes in $P(Y)$), and, in streaming or non-stationary settings, broader forms of *concept/conditional* shift affecting $P(Y | X)$ (Quiñonero-Candela et al., 2008; Gama et al., 2014; Lu et al., 2018). A central practical question is therefore not only whether $Q_X \neq P_X$, but whether the shift

meaningfully affects the behaviour of the model f_θ .

Limitations of current OOD approaches. Out-of-distribution (OOD) detection methods usually approach this question from two complementary angles. *Data-centric* methods model the training marginal P_X and flag inputs that appear unlikely, while methods operate on classifier outputs (e.g. softmax confidence) or learned representations (e.g. feature-space distances); see for example (Hendrycks & Gimpel, 2017; Liang et al., 2018; Liu et al., 2020; Nalisnick et al., 2019). Each captures part of the picture: data-centric scores can detect distribution change but do not specify whether it matters for the task, whereas model-centric scores can reveal brittleness yet do not explicitly connect f_θ to the geometry of the input distribution (Rabanser et al., 2019; Yang et al., 2024). What is missing is a principled mechanism that links the *geometry of the data* to the *sensitivity of the model* in a way that remains usable at test time.

Our perspective: Stein operators. To bridge data geometry and model sensitivity we propose a novel way of using Stein operators. Stein’s method compares a candidate distribution q to a reference distribution p via an operator \mathcal{T}_p satisfying $\mathbb{E}_p[\mathcal{T}_p g] = 0$ for a rich class of test functions g (Stein, 1972; Ley et al., 2017). Departures $\mathbb{E}_q[\mathcal{T}_p g] \neq 0$ certify $q \neq p$. Stein operators underpin discrepancy measures and goodness-of-fit tests such as kernelised Stein discrepancies, and more broadly provide a computational interface between score information and distributional mismatch (Gorham & Mackey, 2015; Liu et al., 2016; Anastasiou et al., 2023). Crucially, most Stein-based discrepancy tests treat g as a free element of a function class and optimise or randomise over it to obtain *distribution-level* tests. In contrast, in deployment we already have a trained model $f_\theta(x) \approx \mathbb{E}[Y | X = x]$, and we are specifically interested in how a distribution shift affects *this* function. This motivates a model-centric question:

What can we say about distribution shift and reliability if we fix the Stein test function to be the deployed predictor f_θ itself?

TASTE: Task-Aware TASTE functional. Fixing the test function f of interest instead of aiming for a result over a wide class of test functions is a novel use of Stein’s method. We use it here to develop **TASTE**, a task-aware framework

¹Department of Statistics, University of Oxford, United Kingdom. Correspondence to: Michał Kozyra <michal.kozyra@seh.ox.ac.uk>.

built around the Langevin Stein operator

$$\mathcal{L}_p f(x) = \Delta f(x) + \nabla \log p(x)^\top \nabla f(x),$$

constructed from a (potentially unnormalised) density/score model p for training data and a fixed $f = f_\theta$. The score $\nabla \log p$ connects the operator to score-based views of data geometry and score-matching models (Song et al., 2021). For each sample X , the value $\mathcal{L}_p f(X)$ gives a *per-sample Stein residual*, with mean 0 under p . We study what we call the *task-aware Stein, or TASTE, functional*

$$S_f(p, q) := \mathbb{E}_q[\mathcal{L}_p f(X)] \quad (1)$$

under a test distribution q which is often approximated by the empirical distribution of the data. Under mild regularity assumptions $S_f(p, q)$ admits an explicit ‘‘projection’’ form,

$$S_f(p, q) = -\mathbb{E}_q\left[\nabla f(X)^\top \nabla \log \frac{q(X)}{p(X)}\right], \quad (2)$$

which can be interpreted as an $L^2(q)$ inner product between the sensitivity field ∇f of the model, and the shift-score field $\nabla \log(q/p)$. Eq.(2) clarifies task-aware nature of the signal: for fixed f , $S_f(p, q)$ responds to the components of distribution shift that influence ∇f in expectation; see Figure 1.

We focus on the Langevin Stein operator as it provides a scalar functional with a geometric interpretation. While simpler first-order Stein operators can also be constructed, they exhibit limitations such as directional blind spots and loss of linear sensitivity; see Appendix G.

Practical appeal of TASTE: plug-and-play, model-agnostic, interpretable. Our approach is *plug-and-play*: at test time it combines any fixed f_θ with any score/density estimator for p and produces an OOD signal without re-training the classifier or requiring negative samples. It is *model-agnostic* in the sense that it only requires access to input-gradients of f_θ (available via autodiff for standard architectures) and an estimate of $\nabla \log p$. Finally, the operator admits a natural *per-input-dimension* decomposition; for images this yields per-pixel residual maps, providing interpretable localisation of task-relevant anomalies and enabling fine-grained diagnostic visualisations.

Contributions. Our main contributions are as follows.

- **TASTE: model-centric Stein diagnostics.** We formalise a task-aware TASTE functional by applying the Langevin Stein operator to a fixed model, and derive a projection identity that links distribution shift to the sensitivity field of the model.
- **Robustness to score-model error.** We analyse how inaccuracies in learned score models affect the proposed methodology and provide a simple correction that removes systematic bias using training data.

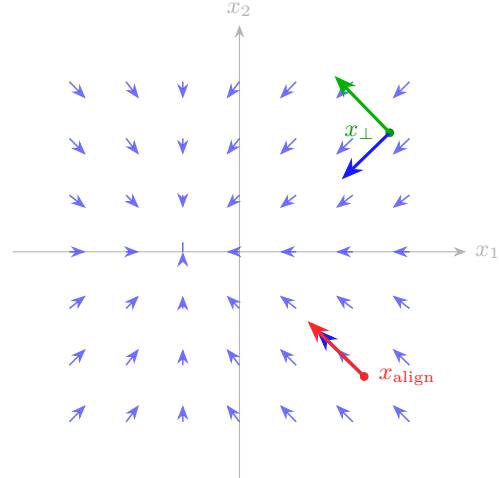


Figure 1. Task-aware intuition behind TASTE. Blue contours depict the score-shift field between the training density $p(x)$ and test density $q(x)$. TASTE measures – without explicit knowledge of q – how distribution shift aligns with the input sensitivity of the model $\nabla f(x)$: shifts aligned with ∇f (red) produce a large response, while orthogonal shifts (green) are largely ignored even if they are large in density terms.

- **Per-sample TASTE scores and interpretable decompositions.** We derive per-sample Stein residuals as OOD scores and show how their coordinate-wise decomposition yields per-input (and per-pixel) anomaly maps for image data.
- **Empirical validation across diverse shift regimes.** We demonstrate that the Stein signal aligns with task degradation in controlled shift models and achieves strong performance against standard OOD baselines on common benchmark suites (including corruption and perturbation benchmarks, mixed in-/out-distribution test sets, and adversarially perturbed inputs).

Scope. The goal of this paper is not to propose yet another OOD score in isolation, but to articulate a general framework in which a fixed f_θ and a density/score model for $p(x)$ are linked via a principled operator. Within this framework, TASTE functionals act as task-aware probes of distribution shift, offering a bridge between generative and discriminative views of uncertainty in deep learning.

2. Related Work

Dataset shift, OOD detection, and evaluation. The dataset-shift literature distinguishes changes in P_X , changes in P_Y , and changes in $P(Y | X)$, and studies both detection and adaptation under non-stationarity (Quiñonero-Candela et al., 2008; Gama et al., 2014; Lu et al., 2018). In modern OOD detection, the dominant focus is on *detecting* atypical test inputs and quantifying separation between in- and out-distribution samples, with a growing emphasis on unified

taxonomies and evaluation protocols (Yang et al., 2024; Rabanser et al., 2019). Our work complements this direction by emphasising *task relevance*: the goal is not to detect all deviations from P_X , but to detect distribution shifts that influence the deployed model.

Data-centric vs. model-centric OOD scoring. Data-centric methods use density or score models to assess novelty under P_X , yet the likelihood can be misaligned with semantic novelty in high-dimensional image data (Nalisnick et al., 2019; Ren et al., 2019). Model-centric methods instead use confidence and calibration heuristics or representation distances, including Maximum Softmax Probability (MSP)-style baselines and methods that shape output energies or logits to improve separability (Hendrycks & Gimpel, 2017; Liang et al., 2018; Liu et al., 2020). Our Stein construction is a hybrid: it uses a learned score model to represent data geometry while explicitly coupling it to the input-sensitivity of the model, yielding a task-aware signal.

Stein’s method in computation and machine learning. Stein operators have been used to construct discrepancy measures and goodness-of-fit tests such as kernelised Stein discrepancies (Liu et al., 2016) and computable measures of sample quality (Gorham & Mackey, 2015), see the survey (Anastasiou et al., 2023) for details and further uses. In contrast to the typical setting which obtains a measure of discrepancy by optimising the TASTE functional (2) over a set of test functions, TASTE fixes the test function, yielding a model-centric diagnostic tool.

Score models and geometric viewpoints. Score matching and diffusion-based generative modelling provide scalable ways to estimate $\nabla \log p(x)$ for complex, high-dimensional data, and can be interpreted geometrically as learning vector fields aligned with local density gradients (Song et al., 2021). This makes score models a natural component in operator-based diagnostics that require access to the data geometry, including our Stein-based construction.

Localisation and per-input diagnostics. Beyond binary OOD detection, many applications require localisation: identifying which features or pixels contribute to abnormality. In computer vision, pixel- level anomaly localisation has been studied extensively (Bergmann et al., 2020; Roth et al., 2022). Separately, feature-level shift localisation aims to identify which coordinates have shifted between train and test distributions (Kulinski et al., 2020). Our TASTE residuals provide a task-aware route to such localisation: they decompose the same operator used for global and per-sample diagnostics into interpretable per-input contributions.

3. Stein operators and data geometry

Here we provide the minimal Stein machinery needed for our goal to connect a *fixed* model f to the geometry of

a reference data distribution p via a differential operator whose expectation vanishes under p . We refer to (Anastasiou et al., 2023) for details. We use the following setting and notation. Let $f : \mathbb{R}^d \rightarrow \mathbb{R}$ be a scalar test function (or predictor); for a vector-valued predictor $f : \mathbb{R}^d \rightarrow \mathbb{R}^m$ we apply all definitions componentwise. We write $\nabla f(x) \in \mathbb{R}^d$ for the gradient and $\Delta f(x) := \sum_{i=1}^d \frac{\partial^2 f(x)}{\partial x_i^2}$ for the Euclidean Laplacian. The divergence of a vector field v is $\nabla \cdot v = \sum_{i=1}^d \partial_{x_i} v_i$.

We assume that $p : \mathbb{R}^d \rightarrow (0, \infty)$ is a continuously differentiable probability density with *score function*

$$s_p(x) := \nabla \log p(x) \in \mathbb{R}^d.$$

The score function requires the density p to be available only up to a normalising constant. Expectations under p are denoted $\mathbb{E}_p[\cdot]$.

A so-called *Stein operator* is an operator \mathcal{L}_p such that $\mathbb{E}_p[\mathcal{L}_p g(X)] = 0$ for a sufficiently rich class of test functions g . Here we focus on the *Langevin Stein operator*

$$\mathcal{L}_p f(x) := \Delta f(x) + s_p(x)^\top \nabla f(x), \quad (3)$$

where f is a smooth scalar function. This operator can be recognised as the infinitesimal generator of a Langevin diffusion for which p is an invariant density, and it provides the standard starting point for kernelised Stein discrepancies and Stein-based goodness-of-fit testing. A key property of \mathcal{L}_p is that it admits a divergence form:

$$\mathcal{L}_p f(x) = \frac{1}{p(x)} \nabla \cdot (p(x) \nabla f(x)). \quad (4)$$

Under mild regularity and boundary decay conditions, see Appendix A.1, the divergence form (4) implies the classical *Stein identity*:

$$\mathbb{E}_p[\mathcal{L}_p f(X)] = 0 \quad (5)$$

holds for any sufficiently regular f . Eq. (5) is the formal reason Stein operators are useful: they produce quantities that equal zero for in-distribution data (in expectation), but become nonzero under distribution shift.

The divergence view (4) also provides a geometric interpretation. The vector field $p(x) \nabla f(x)$ can be seen as a density-weighted *sensitivity flow* induced by the model. The Stein identity states that, under the reference density p , this field cannot generate net flux in expectation. In our setting, this interpretation is particularly natural: ∇f captures local model sensitivity, while p encodes the data geometry; $\mathcal{L}_p f$ combines both into a single scalar diagnostic.

4. TASTE: Task-aware Stein functionals

We now shift from the classical “ f is free” viewpoint in Stein’s method to our model-centric setting: we fix f to be a

pre-trained model and ask how Stein operators behave when the test distribution differs from the training distribution.

4.1. TASTE functionals under a shifted test distribution

Let q be another smooth density on \mathbb{R}^d , absolutely continuous with respect to p , and let $S_f(p, q)$ be the TASTE functional of the fixed predictor f at (p, q) given in (1). When $q = p$, (5) implies $S_f(p, p) = 0$. When $q \neq p$, the functional measures how the test distribution violates the Stein identity that holds under p . A central identity expresses $S_f(p, q)$ directly in terms of the density ratio q/p .

Proposition 4.1 (Projection identity). *Under mild regularity (see Appendix A.2),*

$$S_f(p, q) = -\mathbb{E}_q \left[\nabla f(X)^\top \nabla \log \frac{q(X)}{p(X)} \right]. \quad (6)$$

Defining the *shift score field* $u_{p \rightarrow q}(x) := \nabla \log \frac{q(x)}{p(x)}$, equation (6) becomes $S_f(p, q) = -\langle \nabla f, u_{p \rightarrow q} \rangle_{L^2(q)}$. This is the key “task-aware” mechanism: for a fixed predictor f , the Stein functional measures only the component of the distribution shift that aligns with the predictor’s sensitivity field ∇f . Shifts that are large in density terms but lie mostly in directions orthogonal to ∇f can be invisible to S_f ; conversely, comparatively small shifts can trigger a strong response if they move mass along directions where f is sensitive. This projection view is the mathematical basis for our claim that Stein residuals are *task-aware*.

4.2. Small-change analysis via exponential tilts

To understand the behaviour of $S_f(p, q)$, first we consider smooth perturbations of p via exponential tilts

$$q_\varepsilon(x) = \frac{1}{Z_\varepsilon} p(x) e^{\varepsilon h(x)}, \quad (7)$$

where $h : \mathbb{R}^d \rightarrow \mathbb{R}$ is a shift potential and ε controls the shift strength. Under regularity assumptions on h , we have $\nabla \log \frac{q_\varepsilon(x)}{p(x)} = \varepsilon \nabla h(x)$, and substituting (7) into (6) yields

$$S_f(p, q_\varepsilon) = -\varepsilon \mathbb{E}_{q_\varepsilon} [\nabla f(X)^\top \nabla h(X)]. \quad (8)$$

Moreover, expanding expectations under q_ε around p gives the first-order response

$$S_f(p, q_\varepsilon) = \varepsilon \text{Cov}_p(\mathcal{L}_p f(X), h(X)) + O(\varepsilon^2), \quad (9)$$

and an analogous expansion for $\text{Var}_{q_\varepsilon}[\mathcal{L}_p f(X)]$ (a full derivation and additional assumptions of h are in Appendix A.3). Thus, for small smooth shifts, the TASTE functional responds linearly in ε , with slope given by a covariance under the training distribution. In practice, this regime may provide a useful diagnostic lens even when real shifts are not exactly tilts.

4.3. Correcting for using an approximate score model

Computing $\mathcal{L}_p f$ requires access to $s_p = \nabla \log p$, yet in applications p is unknown and we substitute a learned model \tilde{p} with score $\tilde{s} = \nabla \log \tilde{p}$, yielding the approximate operator

$$\mathcal{L}_{\tilde{p}} f(x) = \Delta f(x) + \tilde{s}(x)^\top \nabla f(x).$$

A useful consequence of the projection identity is that the error induced by \tilde{s} is *directional*: it depends on how score-model error aligns with ∇f and the shift direction q/p .

Concretely, letting $l(x) := q(x)/p(x)$ and placing $g(x) := (\tilde{s}(x) - s_p(x))^\top \nabla f(x)$, under mild regularity assumptions, one obtains the decomposition (see Appendix A.4)

$$\mathbb{E}_q[\mathcal{L}_{\tilde{p}} f] = \mathbb{E}_p[\mathcal{L}_{\tilde{p}} f] + S_f(p, q) + \langle g, l - 1 \rangle_{L^2(p)}, \quad (10)$$

This motivates the *adjusted TASTE functional*

$$\tilde{S}_f(p, q) := \mathbb{E}_q[\mathcal{L}_{\tilde{p}} f] - \mathbb{E}_p[\mathcal{L}_{\tilde{p}} f], \quad (11)$$

where $\mathbb{E}_p[\mathcal{L}_{\tilde{p}} f]$ can be estimated on held-out training data.

The adjusted TASTE functional $\tilde{S}_f(p, q)$ gives rise to several observations. First, it guarantees *no false alarm under no shift*: when $q = p$, the density ratio satisfies $l \equiv 1$ and both $S_f(p, p) = 0$ and $\langle g, l - 1 \rangle_{L^2(p)} = 0$, so the corrected functional vanishes even if the score model \tilde{s}_p is imperfect. Second, the response of $\tilde{S}_f(p, q)$ is inherently *task-aware*. As the error term $\langle g, l - 1 \rangle_{L^2(p)}$ is an inner product in $L^2(p)$, only those distribution shifts whose direction has nonzero projection onto $g(x) = (\tilde{s}_p(x) - s_p(x))^\top \nabla f(x)$ produce a response in expectation; shifts orthogonal to the gradient field of the model are invisible. Third, the influence of score-model mismatch is quantitatively controlled. Since $g(x) = (\tilde{s}_p(x) - s_p(x))^\top \nabla f(x)$, the bias term satisfies

$$|\langle g, l - 1 \rangle_{L^2(p)}| \leq \sqrt{J(p\|\tilde{p})} \|\nabla f\|_{L^4(p)} \|l - 1\|_{L^4(p)}, \quad (12)$$

where $J(p\|\tilde{p})$ is the Fisher divergence minimized by denoising score matching (Song et al., 2021). As long as $\|l - 1\|_{L^4(p)}$ is controlled, improved score estimation translates into tighter bounds for the adjusted TASTE functional.

On access to the test distribution. We do not assume access to an explicit density for the test distribution q . The distribution q enters only implicitly through test samples, and all expectations with respect to q are estimated empirically by sample averages over the observed test set.

4.4. Per-sample and per-dimension residuals

The corrected quantity in (11) can be used at different granularity levels.

Per-sample TASTE scores. Given a test input $x \sim q$, define the adjusted TASTE residual

$$r_f(x) := \mathcal{L}_{\tilde{p}} f(x) - D_f.$$

where $D_f = \mathbb{E}_p[\mathcal{L}_{\tilde{p}}f(X)]$, which in practice is estimated from training data. Per-sample scores such as $|r_f(x)|$ (or signed $r_f(x)$) can be used for OOD ranking, while averages over test sets estimate $\tilde{S}_f(p, q)$.

Per-dimension decomposition and interpretability. Writing derivatives component-wise gives the representation $\mathcal{L}_p f(x) = \sum_{i=1}^d \left(\partial_{ii} f(x) + \partial_i \log p(x) \partial_i f(x) \right)$. This motivates introducing per-dimension *TASTE residuals*

$$r_{f,i}(x) := \partial_{ii} f(x) + \partial_i \log p(x) \partial_i f(x), \quad (\star)$$

so that $r_f(x) = \sum_i r_{f,i}(x)$. Importantly, each coordinate-wise $r_{f,i}(x)$ is itself a valid Langevin Stein operator applied to the one-dimensional test function $x \mapsto \partial_i f(x)$. Under the same regularity conditions as for the full operator, each component satisfies $\mathbb{E}_p[r_{f,i}(X)] = 0$, and admits an analogous projection formula under a shifted distribution. As a result, all theoretical properties established for the aggregated TASTE functional—task-aware sensitivity to shift and robustness via baseline correction—extend directly to the per-dimension setting.

In imaging applications, the index i corresponds to a pixel (or pixel-channel), yielding an interpretable anomaly map $i \mapsto r_{f,i}(x)$. In this sense, TASTE residuals provide a *model-agnostic and interpretable* mechanism: they apply to any pre-trained predictor for which gradients are available, and their per-input¹ decomposition highlights which input coordinates contribute most strongly to the task-aware shift signal (\star). This setting supports use cases such as pixel-level anomaly segmentation and localisation of distributional shift within an image, which have been extensively studied in industrial inspection and medical imaging (Bergmann et al., 2020; Roth et al., 2022; Zenati et al., 2018).

5. TASTE Methodology

Overall, the proposed pipeline is as follows: (i) take any fixed predictor f_θ , (ii) take any score/density model \tilde{p} for p (e.g. a diffusion/score model), (iii) compute $\mathcal{L}_{\tilde{p}}f_\theta(x)$ (exactly or approximately) over the test, (iv) subtract a train-estimated baseline D_f , and (v) use the resulting per-sample or per-dimension residuals for task-aware OOD detection and diagnostics. For details see Algorithm 1

Calibrated testing interpretation. The per-sample Stein residual can also be used to define a simple calibrated OOD test. Using held-out training data, we estimate a threshold τ_α as the empirical $(1 - \alpha)$ -quantile of $|r_f(X)|$ (or signed $r_f(x)$) under $X \sim p$. At test time, an input x is declared out-of-distribution if $|r_f(x)| > \tau_\alpha$. This yields a model-

¹Note that the "per-input" here refers to a single coordinate of the gradient/Laplacian. Evaluating each $r_{f,i}(x)$ requires the entire $x \in \mathbb{R}^n$.

Algorithm 1 Batched Adjusted TASTE Residuals

```

1: Input: test set  $\mathcal{X}_{\text{test}}$ , (optional) calibration set  $\mathcal{X}_{\text{train}}$ , predictor  $f_\theta$ , score model  $\hat{s}_p$ , batch sizes  $B_{\text{train}}, B_{\text{test}}$ , options: compute_D (bool), Hutchinson samples  $K$ 
2: Helper: STEIN_OP_BATCH( $X$ )
3: Compute gradients  $G \leftarrow \nabla f_\theta(X)$  for batch  $X$ 
4: Estimate Laplacians  $L \leftarrow \Delta f_\theta(X)$  for batch  $X$  (exact or Hutchinson with  $K$  samples)
5: Compute batch Stein values  $U \leftarrow L + \hat{s}_p(X)^\top G$  (vector of length  $|X|$ )
6: Return  $U$ 
7: if compute_D is true then
8:    $S \leftarrow 0, n \leftarrow 0$ 
9:   for each training batch  $X_{\text{train},b}$  of size  $B_{\text{train}}$  do
10:     $U_b \leftarrow \text{STEIN\_OP\_BATCH}(X_{\text{train},b})$ 
11:     $S \leftarrow S + \sum U_b, n \leftarrow n + |U_b|$ 
12:   end for
13:    $D_f \leftarrow S/n$ 
14: else
15:    $D_f \leftarrow 0$ 
16: end if
17: Initialize list of scores  $\text{Scores} \leftarrow \emptyset$ 
18: for each test batch  $X_{\text{test},b}$  of size  $B_{\text{test}}$  do
19:    $U_b \leftarrow \text{STEIN\_OP\_BATCH}(X_{\text{test},b})$ 
20:    $R_b \leftarrow U_b - D_f$  (vector of adjusted residuals)
21:   Append  $\{R_b\}$  to  $\text{Scores}$  (or append  $\{|R_b|\}$ )
22: end for
23: Output:  $\text{Scores}$ 

```

agnostic decision rule that approximately controls the false positive rate under the training distribution, while remaining sensitive to shifts that affect the predictor's behaviour.

Aggregation. The per-sample scores returned by Algorithm 1 are often aggregated (e.g. averaged over the test set or used in a batch statistic) to produce a single test-set operator value $\frac{1}{|\mathcal{X}_{\text{test}}|} \sum_{x \in \mathcal{X}_{\text{test}}} r_f(x)$ for global shift detection.

Computational efficiency. Computing the Laplacian term $\Delta f_\theta(x) = \text{tr}(\nabla^2 f_\theta(x))$ exactly is computationally expensive in high dimensions. In practice we therefore rely on stochastic trace estimators, most notably Hutchinson's unbiased estimator and its modern variance-reduced variants (Hutchinson, 1989; Meyer et al., 2021).

Per-dimension residual maps. A per-dimension decomposition computes coordinate-wise terms $r_i(x) = \partial_{ii} f_\theta(x) + \hat{s}_{p,i}(x) \partial_i f_\theta(x)$ for each input dimension i , producing a spatial/feature map $\{r_i(x)\}_{i=1}^d$. If this map is used, the correction D_f must also be estimated as a per-dimension vector $D_f = (\mathbb{E}_p[r_1(X)], \dots, \mathbb{E}_p[r_d(X)])$ (in practice estimated by aggregating per-dimension raw residuals on the calibration set). This per-dimension mode enables fine-grained anomaly heatmaps but increases compute as Hutchinson

approximation cannot be used directly.

On the Laplacian term for ReLU networks. For architectures with a piecewise-affine backbone (e.g. ResNets with ReLU and pooling) followed by a smooth softmax output, classical second derivatives of the backbone vanish almost everywhere. Let $z(x) \in \mathbb{R}^K$ denote the logits and $f_k(x) = \sigma_k(z(x))$ the softmax probabilities. Since $\nabla_x^2 z_i(x) = 0$ a.e., all non-zero curvature of f_k arises from the softmax via the chain rule, yielding $\Delta f_k(x) = \sum_{i,j} \frac{\partial^2 \sigma_k}{\partial z_i \partial z_j} \langle \nabla_x z_i(x), \nabla_x z_j(x) \rangle$. Thus, for such networks the Laplacian can be computed using only first-order input gradients of the logits and the closed-form softmax Hessian, without second-order backpropagation through ReLU or pooling layers. If the model has no smooth output nonlinearity (e.g. regression), the Laplacian vanishes a.e. and may be omitted. For large K , the sum can be restricted to the top- k logits for efficiency.

6. Experimental results

We present concise empirical evidence that (i) the Langevin Stein residual tracks task-relevant shifts, (ii) remains stable under harmless perturbations, and (iii) yields effective per-sample OOD signals in mixed test sets. Full implementation details and additional plots are deferred to Appendix B. Ablations can be found in Appendix E

6.1. Controlled 2D shift: directional sensitivity

We first study a controlled two-dimensional setting in which the direction of the distribution shift can be varied independently of its magnitude. The training distribution is 2D standard Gaussian $p(x) = \mathcal{N}(0, I_2)$ and the test distribution is obtained by translating p by a fixed magnitude $\varepsilon = 10$ along a rotated version of the base direction $u = (1, 1)^\top / \sqrt{2}$, producing $q_\varphi = \mathcal{N}(\varepsilon R_\varphi u, I_2)$, where R_φ denotes the rotation matrix by the angle φ .

The prediction task is $y = x_2 - x_1$, which is invariant to translations along $(1, 1)$ and maximally sensitive along $(1, -1)$. A small ReLU network is trained under p , and we evaluate prediction error, the TASTE functional $S_f(p, q_\varphi)$, and the log-likelihood under p as φ varies.

Figure 2 shows how the Stein signal tracks task degradation precisely: its extrema align with those of the prediction error, while remaining invariant to shifts that leave the task unchanged. This confirms that the TASTE functional responds selectively to task-relevant components of distribution shift.

6.2. MNIST: invariance to translations, sensitivity to rotations

We next evaluate the method on MNIST under geometric perturbations. Convolutional networks are known to ex-

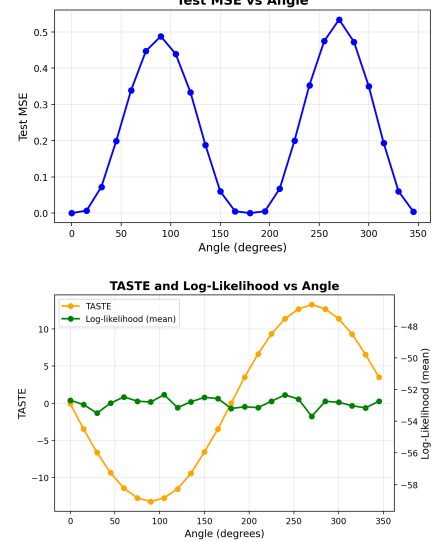


Figure 2. Directional shift experiment. Prediction error and the task-aware Stein signal vary strongly with the direction of shift, peaking (in magnitude) when the shift aligns with the sensitive direction $(1, -1)$. In contrast, the density-based score remains nearly constant for all directions.

hibit approximate translation invariance while remaining sensitive to rotations; we therefore compare translations (largely benign) and rotations (harmful) as test-time shifts. (Hendrycks & Dietterich, 2019; Bronstein et al., 2021).

An AlexNet-style CNN (Krizhevsky et al., 2012) is trained on MNIST. So that translations do not remove semantic content, all images are zero-padded from 28×28 to 64×64 prior to training and evaluation. A denoising score-matching model provides an estimate $\hat{s}_p(x) \approx \nabla \log p(x)$. We compute the adjusted Langevin Stein residual $r_f(x)$ using Algorithm 1. Test sets are constructed using translations of increasing ℓ^∞ magnitude and rotations of increasing angle.

Figure 3 shows that the Stein residual remains near zero under translations but increases sharply under rotations, closely mirroring the drop in accuracy. Likelihood-based scores do not distinguish between these cases, highlighting the task-awareness of the proposed signal.

Consistent with the per-dimension decomposition introduced in the methodology, the Stein residual can also be evaluated coordinate-wise on image inputs. On MNIST, this yields per-pixel residual maps that localise regions most incompatible with the training distribution as processed by the classifier. We defer the visualizations of per-dimension residuals to Appendix D; additional evaluations using a mixed MNIST / Fashion-MNIST OOD setup are found in Appendix F.

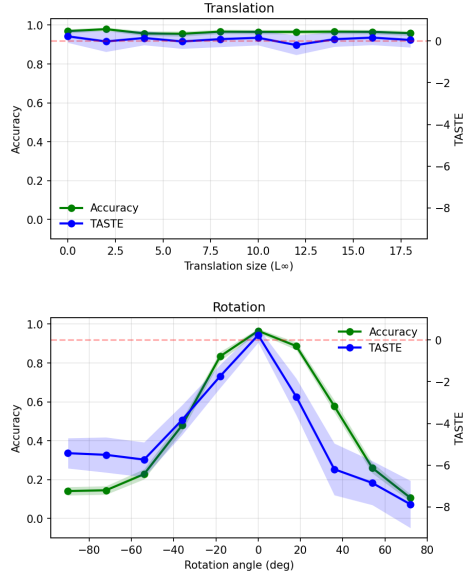


Figure 3. MNIST under geometric perturbations. Top: classification accuracy. Bottom: corresponding Stein signal. Translations (left) leave both accuracy and Stein score unchanged, while rotations (right) induce a monotonic increase in the Stein signal aligned with performance degradation.

6.3. Benchmark evaluation on CIFAR-10

We evaluate the proposed TASTE residual against widely used OOD detection baselines on CIFAR-10, covering heterogeneous shift regimes including adversarial perturbations, synthetic corruption benchmarks, and standard OOD datasets (Krizhevsky, 2009; Yang et al., 2024). The in-distribution data is CIFAR-10, the classifier is a ResNet-18 (He et al., 2016), and the score model is a diffusion-based estimator of $\nabla \log p(x)$ (Ho et al., 2020). Implementation and configuration details are deferred to Appendix B.

Benchmarks. We group evaluation datasets into four categories: (i) *adversarial perturbations*: FGSM, PGD, and AutoAttack (Goodfellow et al., 2014; Madry et al., 2018; Croce & Hein, 2020); (ii) *corruption benchmarks*: CIFAR-10-C, averaged over all corruption types; (iii) *perturbation benchmarks*: CIFAR-10-P, averaged over all perturbation types (Hendrycks & Dietterich, 2019); and (iv) *classical OOD datasets*: SVHN, LSUN, iSUN, Textures, and Places365 (Netzer et al., 2011; Yu et al., 2016; Xu et al., 2015; Cimpoi et al., 2014; Zhou et al., 2017). All results are reported using AUROC and false positive rate at 95% true positive rate (FPR95), averaged within each category.

Baselines. We compare against representative confidence-based, distance-based, and energy-based OOD detectors, including MSP (Hendrycks & Gimpel, 2017), ODIN (Liang et al., 2018), Mahalanobis distance (Lee et al., 2018), energy scores (Liu et al., 2020), kNN-based methods (Sun et al., 2022), and Gradient Short-Circuit (Gu et al., 2025). Details

are provided in Appendix B.

Results and benchmark analysis. Table 1 reports OOD detection performance across adversarial attacks, corruption-based shifts (CIFAR-10-C), structured perturbations (CIFAR-10-P), and classical OOD benchmarks. Consistent with prior work, no single method dominates across all regimes (Tajwar et al., 2021). TASTE exhibits a consistent and competitive profile. It achieves the strongest overall average performance, with particularly low FPR95, indicating improved reliability in low-false-positive regimes. On adversarial attacks—where MSP and ODIN degrade substantially, TASTE outperforms confidence-, representation-, and distance-based methods, indicating sensitivity to task-relevant perturbations even when classifier confidence remains high. On CIFAR-10-C and CIFAR-10-P, performance is competitive with strong representation-based methods, consistent with the fact that many corruptions only partially interact with the classifier’s decision boundaries. On standard OOD benchmarks, Stein residuals achieve the lowest average FPR95, even when AUROC differences are modest.

6.4. Per-pixel anomaly detection on MVTec AD

Evaluation on MVTec AD. We evaluate per-pixel TASTE residuals on the MVTec Anomaly Detection dataset to assess spatial localisation on high-resolution real-world imagery. MVTec AD is used for localisation-focused evaluation and ablations, as it provides pixel-level ground-truth annotations supporting both quantitative metrics (pixel-level AUROC, average precision, AUPRO) and visual inspection. Our goal is not to compete with specialised industrial detectors, but to demonstrate that TASTE produces meaningful, spatially coherent localisation signals in a fully *zero-shot* setting: neither the classifier nor the score model is trained or fine-tuned on MVTec AD data.

For each test image, we compute per-pixel Stein heatmaps from the coordinate-wise operator and compare them to ground-truth defect masks. Across categories, the heatmaps align spatially with defect regions. Representative examples are shown in Appendix D.

Quantitative localisation results. Next we report standard image- and pixel-level localisation metrics. Averaged over all 15 MVTec categories, TASTE achieves an image-level AUROC of 0.6527 and average precision of 0.817, indicating consistent image-level separability in a zero-shot regime. At the pixel level, performance reaches an AUROC of 0.6977 and an AUPRO of 0.688.

Performance varies across category types. Texture categories exhibit substantially stronger localisation (pixel-level AUROC 0.8682, AUPRO 0.8745), while object categories are more challenging (AUROC 0.6124, AUPRO 0.5947).

Overall, these results confirm that TASTE produces mean-

Table 1. OOD detection performance on CIFAR-10 across heterogeneous shift regimes.

Method	Adversarial		CIFAR-10-C		CIFAR-10-P		OOD-benchmarks		Overall	
	AUROC↑	FPR95↓	AUROC↑	FPR95↓	AUROC↑	FPR95↓	AUROC↑	FPR95↓	AUROC↑	FPR95↓
MSP	0.3575	0.9656	0.6124	0.9109	0.5978	0.9210	0.8032	0.7878	0.5734	0.9127
ODIN	0.4895	0.9436	0.5499	0.9013	0.5478	0.9222	0.7644	0.7756	0.5598	0.9018
Mahalonobis	0.5819	0.8388	0.5880	0.9181	0.5620	0.9435	0.8188	0.7195	0.6060	0.8846
Energy	0.3550	0.9681	0.6256	0.8900	0.6110	0.9113	0.8520	0.6683	0.5871	0.9018
kNN+	0.4645	0.9591	0.6151	0.8977	0.5956	0.9223	0.8288	0.7023	0.6006	0.8957
GSC	0.5593	0.9250	0.6047	0.8580	0.5959	0.8635	0.7429	0.7855	0.6078	0.8662
TASTE (ours)	0.6144	0.865	0.6193	0.8691	0.5954	0.8611	0.7647	0.5677	0.6285	0.8263

Results are averaged within each category. Adversarial attacks include FGSM, PGD, and AutoAttack. CIFAR-10-C and CIFAR-10-P report averages over all corruption and perturbation types, respectively. OOD benchmarks include SVHN, LSUN, iSUN, Textures, and Places365. Detailed decompaction of each data category and more granular results are presented in the Appendix C.

ingful, spatially structured anomaly signals without task-specific training. While not designed to match state-of-the-art industrial detectors, the method provides a principled zero-shot localisation mechanism whose behaviour is transparent and consistent with the theoretical analysis.

7. Discussion and Conclusion

We introduced TASTE, a task-aware OOD detection framework that applies Stein operators to fixed, deployed predictors. By coupling model input sensitivity with a learned score of the training distribution, TASTE yields OOD signals that align with task degradation and admit interpretable per-sample and per-input decompositions. Across controlled shifts and standard benchmarks, the method achieves competitive performance while providing diagnostic capabilities unavailable to purely confidence-based approaches.

TASTE provides a task-aware lens on distribution shift by explicitly linking the input sensitivity of a fixed predictor to the geometry of the training distribution via Stein operators. Rather than detecting all deviations from the data distribution, the resulting residuals respond selectively to shifts that influence the model, offering a useful perspective for reliability analysis and post-deployment monitoring. This framing is particularly relevant in security-critical settings, where benign covariate changes and harmful task-level perturbations must be distinguished.

Limitations. The approach remains constrained by the quality of the underlying score model, the cost of estimating differential operators, and the fact that Stein identities hold in expectation—so pointwise residuals may exhibit nontrivial variance. These limitations do not undermine the conceptual framework, but highlight practical considerations: accuracy of the generative model affects signal fidelity, differential estimators influence stability, and care is needed when interpreting per-sample statistics.

Choice of Stein operator. Different Stein operators en-

code different geometric notions of compatibility between a predictor and a data distribution. The Langevin operator captures curvature and drift alignment via second-order information, while the first-order operator and its L^2 -norm variant emphasise gradient-score alignment and are computationally lighter. The choice of operator therefore reflects what type of interaction between the predictor and the input distribution one wishes to probe: curvature-based, gradient-based, or score-weighted smoothness, echoing broader geometric perspectives on representation and invariance in deep learning (Bronstein et al., 2021).

Reversing the perspective. Rather than beginning with a predefined Stein operator and analysing its effect, one may instead start from a desired interaction between the shift score $\nabla \log(q/p)$ and some function of the model (e.g. its gradient, curvature, or feature map) and then construct the corresponding Stein operator. This “design-by-intent” viewpoint opens the door to customised task-aware operators tailored to particular vulnerabilities, architectures, or modalities (Mijoule et al., 2023).

Future directions. Promising avenues include developing lower-variance and lower-cost approximations to Stein operators, understanding how to choose operators in a principled task-dependent way, and extending the framework toward kernelised Stein discrepancies to capture richer functional classes (Mijoule et al., 2023) or operate in feature space. These directions may further connect Stein-based diagnostics to established OOD detection pipelines, adversarial robustness evaluations, and model auditing tools.

Overall, this work positions Stein operators as practical, plug-and-play tools for task-aware monitoring of deployed models, bridging generative information about the data distribution with discriminative model sensitivity. We hope this perspective motivates further exploration of task-aware operator design, scalable approximations, and applications to robustness, auditing, and security-critical model monitoring.

Impact Statement

This paper presents work whose goal is to advance the field of Machine Learning. There are many potential societal consequences of our work, none which we feel must be specifically highlighted here.

References

Anastasiou, A., Barp, A., Briol, F.-X., Ebner, B., Gaunt, R. E., Ghaderinezhad, F., Gorham, J., Gretton, A., Ley, C., Liu, Q., et al. Stein’s method meets computational statistics: A review of some recent developments. *Statistical Science*, 38(1):120–139, 2023.

Bergmann, P., Fauser, M., Sattlegger, D., and Steger, C. Uninformed students: Student-teacher anomaly detection with discriminative latent embeddings. In *2020 IEEE/CVF Conference on Computer Vision and Pattern Recognition (CVPR)*, pp. 4182–4191. IEEE, 2020.

Bronstein, M. M., Bruna, J., Cohen, T., and Veličković, P. Geometric deep learning: Grids, groups, graphs, geodesics, and gauges. *arXiv preprint arXiv:2104.13478*, 2021.

Cimpoi, M., Maji, S., Kokkinos, I., Mohamed, S., and Vedaldi, A. Describing textures in the wild. In *Proceedings of the IEEE Conference on Computer Vision and Pattern Recognition*, pp. 3606–3613, 2014.

Croce, F. and Hein, M. Reliable evaluation of adversarial robustness with an ensemble of diverse parameter-free attacks. In *International Conference on Machine Learning*, pp. 2206–2216. PMLR, 2020.

Gama, J., Žliobaitė, I., Bifet, A., Pechenizkiy, M., and Bouchachia, A. A survey on concept drift adaptation. *ACM Comput. Surv.*, 46(4):44:1–44:37, March 2014. ISSN 0360-0300. doi: 10.1145/2523813.

Goodfellow, I. J., Shlens, J., and Szegedy, C. Explaining and harnessing adversarial examples. *arXiv preprint arXiv:1412.6572*, 2014.

Gorham, J. and Mackey, L. Measuring sample quality with stein’s method. *Advances in Neural Information Processing Systems*, 28, 2015.

Gu, J., Qiao, Z., and Li, Z. Gradient short-circuit: Efficient out-of-distribution detection via feature intervention. *arXiv preprint arXiv:2507.01417*, 2025.

He, K., Zhang, X., Ren, S., and Sun, J. Deep residual learning for image recognition. In *Proceedings of the IEEE Conference on Computer Vision and Pattern Recognition*, pp. 770–778, 2016.

Hendrycks, D. and Dietterich, T. Benchmarking neural network robustness to common corruptions and perturbations. *arXiv preprint arXiv:1903.12261*, 2019.

Hendrycks, D. and Gimpel, K. A baseline for detecting misclassified and out-of-distribution examples in neural networks. In *International Conference on Learning Representations*, 2017.

Ho, J., Jain, A., and Abbeel, P. Denoising diffusion probabilistic models. *Advances in Neural Information Processing Systems*, 33:6840–6851, 2020.

Hutchinson, M. A Stochastic Estimator of the Trace of the Influence Matrix for Laplacian Smoothing Splines. *Communications in Statistics - Simulation and Computation*, 18(3):1059–1076, January 1989. ISSN 0361-0918. doi: 10.1080/0360918908812806.

Kingma, D. and Ba, J. Adam: A method for stochastic optimization. *arXiv preprint arXiv:1412.6980*, 2014.

Kirchheim, K., Filax, M., and Ortmeier, F. Pytorch-ood: A library for out-of-distribution detection based on pytorch. In *Proceedings of the IEEE/CVF Conference on Computer Vision and Pattern Recognition*, pp. 4351–4360, 2022.

Krizhevsky, A. Learning multiple layers of features from tiny images. *Master’s thesis, University of Toronto*, 2009.

Krizhevsky, A., Sutskever, I., and Hinton, G. E. ImageNet Classification with Deep Convolutional Neural Networks. In *Advances in Neural Information Processing Systems*, volume 25. Curran Associates, Inc., 2012.

Kulinski, S., Bagchi, S., and Inouye, D. I. Feature shift detection: Localizing which features have shifted via conditional distribution tests. *Advances in Neural Information Processing Systems*, 33:19523–19533, 2020.

Lee, K., Lee, K., Lee, H., and Shin, J. A simple unified framework for detecting out-of-distribution samples and adversarial attacks. *Advances in Neural Information Processing Systems*, 31, 2018.

Ley, C., Reinert, G., and Swan, Y. Stein’s method for comparison of univariate distributions. *Probability Surveys*, 14:1–52, 2017.

Liang, S., Li, Y., and Srikant, R. Enhancing the reliability of out-of-distribution image detection in neural networks. In *International Conference on Learning Representations*, 2018.

Liu, Q., Lee, J., and Jordan, M. A kernelized stein discrepancy for goodness-of-fit tests. In *International Conference on Machine Learning*, pp. 276–284. PMLR, 2016.

Liu, W., Wang, X., Owens, J., and Li, Y. Energy-based out-of-distribution detection. *Advances in Neural Information Processing Systems*, 33:21464–21475, 2020.

Lu, J., Liu, A., Dong, F., Gu, F., Gama, J., and Zhang, G. Learning under concept drift: A review. *IEEE Transactions on Knowledge and Data Engineering*, 31(12):2346–2363, 2018.

Madry, A., Makelov, A., Schmidt, L., Tsipras, D., and Vladu, A. Towards deep learning models resistant to adversarial attacks. In *International Conference on Learning Representations*, 2018.

Meyer, R. A., Musco, C., Musco, C., and Woodruff, D. P. Hutch++: Optimal stochastic trace estimation. In *Symposium on Simplicity in Algorithms (SOSA)*, pp. 142–155. SIAM, 2021.

Mijoule, G., Raič, M., Reinert, G., and Swan, Y. Stein’s density method for multivariate continuous distributions. *Electronic Journal of Probability*, 28:1–40, 2023.

Nalisnick, E., Matsukawa, A., Teh, Y., Gorur, D., and Lakshminarayanan, B. Do deep generative models know what they don’t know? In *International Conference on Learning Representations*, 2019.

Netzer, Y., Wang, T., Coates, A., Bissacco, A., Wu, B., Ng, A. Y., et al. Reading digits in natural images with unsupervised feature learning. In *NIPS Workshop on Deep Learning and Unsupervised Feature Learning*, 2011.

Quiñonero-Candela, J., Sugiyama, M., Schwaighofer, A., Lawrence, N. D., Jordan, M. I., and Dietterich, T. (eds.). *Dataset Shift in Machine Learning*. Neural Information Processing Series. MIT Press, Cambridge, MA, USA, December 2008.

Rabanser, S., Günnemann, S., and Lipton, Z. Failing loudly: An empirical study of methods for detecting dataset shift. *Advances in Neural Information Processing Systems*, 32, 2019.

Ren, J., Liu, P. J., Fertig, E., Snoek, J., Poplin, R., Depristo, M., Dillon, J., and Lakshminarayanan, B. Likelihood ratios for out-of-distribution detection. *Advances in Neural Information Processing Systems*, 32, 2019.

Roth, K., Pemula, L., Zepeda, J., Schölkopf, B., Brox, T., and Gehler, P. Towards total recall in industrial anomaly detection. In *Proceedings of the IEEE/CVF Conference on Computer Vision and Pattern Recognition*, pp. 14318–14328, 2022.

Song, Y., Sohl-Dickstein, J., Kingma, D. P., Kumar, A., Ermon, S., and Poole, B. Score-based generative modeling through stochastic differential equations. In *International Conference on Learning Representations*, 2021.

Stein, C. A bound for the error in the normal approximation to the distribution of a sum of dependent random variables. In *Proceedings of the sixth Berkeley Symposium on Mathematical Statistics and Probability, volume 2: Probability Theory*, volume 6, pp. 583–603. University of California Press, 1972.

Sun, Y., Ming, Y., Zhu, X., and Li, Y. Out-of-distribution detection with deep nearest neighbors. In *International Conference on Machine Learning*, pp. 20827–20840. PMLR, 2022.

Tajwar, F., Kumar, A., Xie, S. M., and Liang, P. No true state-of-the-art? ood detection methods are inconsistent across datasets. *arXiv preprint arXiv:2109.05554*, 2021.

Xu, P., Ehinger, K. A., Zhang, Y., Finkelstein, A., Kulkarni, S. R., and Xiao, J. TurkerGaze: Crowdsourcing saliency with webcam based eye tracking. *arXiv preprint arXiv:1504.06755*, 2015.

Yang, J., Zhou, K., Li, Y., and Liu, Z. Generalized out-of-distribution detection: A survey. *International Journal of Computer Vision*, 132:5635–5662, 2024.

Yu, F., Seff, A., Zhang, Y., Song, S., Funkhouser, T., and Xiao, J. LSUN: Construction of a large-scale image dataset using deep learning with humans in the loop. *arXiv preprint arXiv:1506.03365*, 2016.

Zenati, H., Romain, M., Foo, C.-S., Lecouat, B., and Chandrasekhar, V. Adversarially learned anomaly detection. In *2018 IEEE International Conference on Data Mining (ICDM)*, pp. 727–736. IEEE, 2018.

Zhou, B., Lapedriza, A., Torralba, A., and Oliva, A. Places: An image database for deep scene understanding. *Journal of Vision*, 17(10):296–296, 2017.

A. Core methodology: assumptions, proofs and additional Stein identities

For convenience, this section of the Appendix is structured as follows.

- Appendix A.1: Assumptions and proof of the Stein identity (5) under p ;
- Appendix A.2: Assumptions and proof of the projection identity Proposition 4.1 used to interpret $S_f(p, q)$;
- Appendix A.3: Assumptions and proof of the controlled small-shift expansion (9) for exponential tilts;
- Appendix A.4: Assumptions and proof of the score-model error decomposition (10);
- Appendix A.5: Assumptions and proof for the score-model error stability (12).

A.1. Stein identity for the Langevin operator

Let $f : \mathbb{R}^d \rightarrow \mathbb{R}$ be twice differentiable. Recall the Langevin Stein operator acting on f by

$$\mathcal{L}_p f(x) = \Delta f(x) + (\nabla \log p(x))^\top \nabla f(x) = \frac{1}{p(x)} \nabla \cdot (p(x) \nabla f(x)).$$

Definition A.1 (Stein class for \mathcal{L}_p). Let p be a continuously differentiable density on \mathbb{R}^d . A function $f : \mathbb{R}^d \rightarrow \mathbb{R}$ belongs to the Stein class of p (for \mathcal{L}_p), denoted $f \in \mathcal{F}(p)$, if:

(S1) f is twice continuously differentiable and $\Delta f, \nabla f$ are locally integrable with respect to Lebesgue measure.
 (S2) The vector field $p(x) \nabla f(x)$ is integrable and its flux over spheres vanishes:

$$\lim_{R \rightarrow \infty} \int_{\partial B_R} p(x) \nabla f(x) \cdot n(x) dS(x) = 0,$$

where $B_R \subset \mathbb{R}^d$ is the Euclidean ball of radius R in \mathbb{R}^d , and $n(x)$ is the outward unit normal.

(S3) $\mathcal{L}_p f$ is integrable under p .

Proposition A.2 (Stein identity). *If p is continuously differentiable and $f \in \mathcal{F}(p)$, then*

$$\mathbb{E}_p[\mathcal{L}_p f(X)] = 0.$$

Proof. By ((S3)), $\mathbb{E}_p[\mathcal{L}_p f(X)]$ exists. Using the divergence form,

$$\mathbb{E}_p[\mathcal{L}_p f(X)] = \int_{\mathbb{R}^d} p(x) \mathcal{L}_p f(x) dx = \int_{\mathbb{R}^d} \nabla \cdot (p(x) \nabla f(x)) dx = \lim_{R \rightarrow \infty} \int_{B_R} \nabla \cdot (p(x) \nabla f(x)) dx,$$

where B_R is the ball of radius R , as above. By the divergence theorem,

$$\int_{B_R} \nabla \cdot (p \nabla f) dx = \int_{\partial B_R} p(x) \nabla f(x) \cdot n(x) dS(x).$$

Letting $R \rightarrow \infty$ and using ((S2)) yields $\int_{\mathbb{R}^d} \nabla \cdot (p \nabla f) dx = 0$, hence $\mathbb{E}_p[\mathcal{L}_p f] = 0$. \square

A.2. Proof of the projection identity (Proposition 4.1)

We prove the identity

$$S_f(p, q) = -\mathbb{E}_q \left[\nabla f(X)^\top \nabla \log \frac{q(X)}{p(X)} \right]$$

under sufficient regularity conditions.

Assumption A.3 (Regularity for the projection identity). Let p, q be continuously differentiable densities on \mathbb{R}^d with q absolutely continuous w.r.t. p and let $l(x) = q(x)/p(x)$. Assume:

- (P1) $f \in \mathcal{F}(p)$;
- (P2) $\mathcal{L}_p f \in L^1(q)$;
- (P3) l is differentiable and $p \nabla(f l)$ is integrable.
- (P4) The boundary flux vanishes for the vector field $p l \nabla f$:

$$\lim_{R \rightarrow \infty} \int_{\partial B_R} p(x) l(x) \nabla f(x) \cdot n(x) dS(x) = 0.$$

- (P5) The product $\nabla f^\top \nabla l$ is integrable under Lebesgue measure.

For convenience, we give a full statement of Proposition 4.1.

Proposition 4.1[Projection identity] *Let p, q and f satisfy (P1)–(P5). Then*

$$S_f(p, q) = -\mathbb{E}_q \left[\nabla f(X)^\top \nabla \log \frac{q(X)}{p(X)} \right].$$

Proof of Proposition 4.1. Let p, q and f be such that (P1) – (P4) are satisfied. From (P1), $\mathcal{L}_p f$ exists, and from (P2), $S_f(p, q)$ exists. Substituting $q = lp$ in the divergence form (4) gives

$$S_f(p, q) = \int_{\mathbb{R}^d} q(x) \mathcal{L}_p f(x) dx = \int_{\mathbb{R}^d} l(x) \nabla \cdot (p(x) \nabla f(x)) dx.$$

Integrating by parts, which is justified by (P3) and (P5), using the product rule in the divergence form yields

$$\int_{\mathbb{R}^d} l \nabla \cdot (p \nabla f) dx = \int_{\mathbb{R}^d} \nabla \cdot (l p \nabla f) dx - \int_{\mathbb{R}^d} p \nabla f^\top \nabla l dx.$$

By (P4) and the divergence theorem, the first term on the right-hand side vanishes; hence

$$S_f(p, q) = - \int_{\mathbb{R}^d} p(x) \nabla f(x)^\top \nabla l(x) dx.$$

Now we use $\nabla l = l \nabla \log l$ to obtain

$$S_f(p, q) = - \int_{\mathbb{R}^d} p(x) l(x) \nabla f(x)^\top \nabla \log l(x) dx = - \int_{\mathbb{R}^d} q(x) \nabla f(x)^\top \nabla \log \frac{q(x)}{p(x)} dx,$$

which is the desired identity. \square

A.3. Exponential-tilt expansions and remainder control

We derive the small- ε expansions used in (9). First, we formally state the result.

Proposition A.4. *Let p be a continuously differentiable probability density on \mathbb{R}^d , and let $q_\varepsilon(x)$ be its exponential tilt by a measurable function h*

$$q_\varepsilon(x) = \frac{1}{Z_\varepsilon} p(x) e^{\varepsilon h(x)}.$$

Assume the following:

- (i) *There exists $\delta > 0$ such that $\mathbb{E}_p[e^{\gamma|h(X)|}] < \infty$ for all $|\gamma| < \delta$.*
- (ii) *The Langevin Stein operator satisfies $\mathcal{L}_p f \in L^2(p)$.*

Then, for all positive ε such that $\varepsilon < \delta/4$, the following expansions hold:

$$S_f(p, q_\varepsilon) = \varepsilon \text{Cov}_p(\mathcal{L}_p f(X), h(X)) + O(\varepsilon^2), \quad (13)$$

$$\begin{aligned} \text{Var}_{q_\varepsilon}[\mathcal{L}_p f(X)] &= \text{Var}_p[\mathcal{L}_p f(X)] \\ &+ \varepsilon \text{Cov}_p((\mathcal{L}_p f(X))^2, h(X)) + O(\varepsilon^2). \end{aligned} \quad (14)$$

Proof. Our goal is to expand $\mathbb{E}_{q_\varepsilon}[g(X)]$ and $\text{Var}_{q_\varepsilon}[g(X)]$ for small ε . We proceed in several steps.

Expansion of $\mathbb{E}_{q_\varepsilon}[g(X)]$. Let $g(X) = \mathcal{L}_p f(X)$, which is square-integrable under p by assumption. By definition of the exponential tilt,

$$\mathbb{E}_{q_\varepsilon}[g(X)] = \frac{\mathbb{E}_p[g(X)e^{\varepsilon h(X)}]}{\mathbb{E}_p[e^{\varepsilon h(X)}]}. \quad (15)$$

Under the assumptions stated in the proposition, we shall prove below that

$$\mathbb{E}_p[g(X)e^{\varepsilon h(X)}] = \mathbb{E}_p[g(X)] + \varepsilon \mathbb{E}_p[g(X)h(X)] + O(\varepsilon^2), \quad (16)$$

and similarly,

$$\mathbb{E}_p[e^{-\varepsilon h(X)}] = 1 - \varepsilon \mathbb{E}_p[h(X)] + O(\varepsilon^2). \quad (17)$$

For now we assume that these expansions hold, in order to preserve the flow of the argument. The detailed derivation is deferred to the end of this subsection. Multiplying the numerator and denominator expansions yields with (15) that

$$\mathbb{E}_{q_\varepsilon}[g(X)] = \mathbb{E}_p[g(X)] + \varepsilon \left(\mathbb{E}_p[g(X)h(X)] - \mathbb{E}_p[g(X)] \mathbb{E}_p[h(X)] \right) + O(\varepsilon^2),$$

which is exactly

$$\mathbb{E}_{q_\varepsilon}[g(X)] = \mathbb{E}_p[g(X)] + \varepsilon \text{Cov}_p(g(X), h(X)) + O(\varepsilon^2).$$

Applying the same argument with $g(X)^2$ in place of $g(X)$ yields

$$\mathbb{E}_{q_\varepsilon}[g(X)^2] = \mathbb{E}_p[g(X)^2] + \varepsilon \text{Cov}_p(g(X)^2, h(X)) + O(\varepsilon^2).$$

Specialisation to the Stein quantity $g = \mathcal{L}_p f$. Plugging in $g = \mathcal{L}_p f$ we obtain the deterministic expansions

$$\mathbb{E}_{q_\varepsilon}[\mathcal{L}_p f(X)] = \varepsilon \text{Cov}_p(\mathcal{L}_p f(X), h(X)) + O(\varepsilon^2),$$

and

$$\mathbb{E}_{q_\varepsilon}[(\mathcal{L}_p f(X))^2] = \mathbb{E}_p[(\mathcal{L}_p f(X))^2] + \varepsilon \text{Cov}_p((\mathcal{L}_p f(X))^2, h(X)) + O(\varepsilon^2).$$

Since the mean is $O(\varepsilon)$, its square is $O(\varepsilon^2)$, hence

$$\text{Var}_{q_\varepsilon}[\mathcal{L}_p f(X)] = \text{Var}_p[\mathcal{L}_p f(X)] + \varepsilon \text{Cov}_p((\mathcal{L}_p f(X))^2, h(X)) + O(\varepsilon^2).$$

Proof of First-Order Expansion of $\mathbb{E}[ge^{\varepsilon h}]$.

It now remains to prove the expressions (16) and (17) used above. We begin with the Taylor expansion of the exponential function $f(y) = e^y$ around $y = 0$. For any real scalar $y \in \mathbb{R}$, we have:

$$e^y = 1 + y + R(y),$$

where the remainder term $R(y)$ is bounded by the Lagrange error bound:

$$|R(y)| \leq \frac{y^2}{2} e^{|y|}. \quad (18)$$

For any fixed vector x , let $y = \varepsilon h(x)$. Substituting this into the expression above and multiplying by $g(x)$, we obtain:

$$g(x)e^{\varepsilon h(x)} = g(x) \left(1 + \varepsilon h(x) + R(\varepsilon h(x)) \right) = g(x) + \varepsilon g(x)h(x) + g(x)R(\varepsilon h(x)).$$

Taking the expectations:

$$\mathbb{E}_p[g(x)e^{\varepsilon h(x)}] = \mathbb{E}_p[g(x)] + \varepsilon \mathbb{E}_p[g(x)h(x)] + \mathbb{E}_p[g(x)R(\varepsilon h(x))]. \quad (19)$$

We next show that the remainder term $E_{\text{err}} = \mathbb{E}_p[g(x)R(\varepsilon h(x))]$ satisfies $|E_{\text{err}}| \leq C\varepsilon^2$ for some constant C . Using the bound from (18):

$$|E_{\text{err}}| \leq \mathbb{E}_p[|g(x)| \cdot |R(\varepsilon h(x))|] \leq \mathbb{E}_p\left[|g(x)| \frac{\varepsilon^2 h(x)^2}{2} e^{\varepsilon|h(x)|}\right].$$

Factoring out constants:

$$|E_{\text{err}}| \leq \frac{\varepsilon^2}{2} \mathbb{E}_p\left[|g(x)|h(x)^2 e^{\varepsilon|h(x)|}\right].$$

We now apply the Cauchy-Schwarz inequality to bound the expectation:

$$\mathbb{E}_p\left[|g(x)|\left(h(x)^2 e^{\varepsilon|h(x)|}\right)\right] \leq \|g\|_{L^2(p)} \cdot \|h^2 e^{\varepsilon|h|}\|_{L^2(p)}.$$

We note that $\|g\|_{L^2(p)}$ is finite by assumption. It remains to show that the second term is bounded. The norm is given by:

$$\|h^2 e^{\varepsilon|h|}\|_{L^2(p)} = \left(\mathbb{E}_p[h(x)^4 e^{2\varepsilon|h(x)|}]\right)^{1/2}.$$

By the exponential-integrability assumption, the moment generating function of the scalar random variable $|h(X)|$ exists in a neighbourhood of zero, which in particular implies the finiteness of all polynomial moments of h under p . Moreover, exponential integrability allows control of mixed polynomial-exponential moments. Fix $\varepsilon > 0$ sufficiently small, for instance $\varepsilon < \delta/4$. Applying the Cauchy-Schwarz inequality, we obtain

$$\mathbb{E}_p[h(X)^4 e^{2\varepsilon|h(X)|}] \leq (\mathbb{E}_p[h(X)^8])^{1/2} (\mathbb{E}_p[e^{4\varepsilon|h(X)|}])^{1/2}.$$

Since $\varepsilon < \delta/4$, the exponential-integrability assumption on h implies $\mathbb{E}_p[e^{4\varepsilon|h(X)|}] < \infty$, and exponential integrability also ensures $\mathbb{E}_p[h(X)^8] < \infty$. Consequently, the mixed moment $\mathbb{E}_p[h(X)^4 e^{2\varepsilon|h(X)|}]$ is finite for all $\varepsilon < \delta/4$, justifying the uniform remainder bound used in (16). Expansion (17) follows similarly by using the expansion $e^{-\varepsilon h(x)} = 1 - \varepsilon h(x) + \tilde{R}(\varepsilon h(x))$.

For completeness, we state the explicit bound. Let $K = \|g\|_{L^2(p)} \cdot \|h^2 e^{\varepsilon|h|}\|_{L^2(p)} < \infty$. Then:

$$|E_{\text{err}}| \leq \frac{K}{2} \varepsilon^2.$$

Thus, $E_{\text{err}} = O(\varepsilon^2)$, completing the proof. \square

A.4. Directional score-model error decomposition

Here we provide the full derivation of (10) and the tilt-specialisation used in the main text.

Let \tilde{p} be a learned density model with score $\tilde{s}(x) = \nabla \log \tilde{p}(x)$. Define

$$\mathcal{L}_{\tilde{p}} f(x) := \Delta f(x) + \tilde{s}(x)^\top \nabla f(x), \quad g(x) := (\tilde{s}(x) - s_p(x))^\top \nabla f(x), \quad l(x) := \frac{q(x)}{p(x)}.$$

Proposition A.5 (Directional decomposition). *Assume that p is a continuously differentiable probability density, that q is absolutely continuous w.r.t. p , that $f \in \mathcal{F}(p) \cap \mathcal{F}(q)$, and that $\mathcal{L}_{\tilde{p}} f$ and g are integrable under both p and q . Then*

$$\mathbb{E}_q[\mathcal{L}_{\tilde{p}} f] = \mathbb{E}_p[\mathcal{L}_{\tilde{p}} f] + S_f(p, q) + \mathbb{E}_p[g(X)(l(X) - 1)].$$

Proof. We begin with the decomposition

$$\mathcal{L}_{\tilde{p}} f = \mathcal{L}_p f + (\tilde{s} - \nabla \log p)^\top \nabla f,$$

which is valid for all $f \in \mathcal{F}(p) \cap \mathcal{F}(q)$. Taking expectations under q and p and subtracting gives

$$\mathbb{E}_q[\mathcal{L}_{\tilde{p}}f] - \mathbb{E}_p[\mathcal{L}_{\tilde{p}}f] = \mathbb{E}_q[\mathcal{L}_p f] + \left(\mathbb{E}_q - \mathbb{E}_p\right)[(\tilde{s} - \nabla \log p)^\top \nabla f].$$

Here we used the Stein identity, Proposition A.2. The first term on the right-hand side is $S_f(p, q)$ by definition. For the second term, write $q(x) = l(x)p(x)$ with $l = q/p$, giving

$$\left(\mathbb{E}_q - \mathbb{E}_p\right)[g(X)] = \mathbb{E}_p[g(X)(l(X) - 1)],$$

where $g(x) = (\tilde{s}(x) - \nabla \log p(x))^\top \nabla f(x)$. This yields (10).

For the exponential-tilt case $q_\varepsilon(x) \propto p(x)e^{\varepsilon h(x)}$, the expansion follows directly from the change-of-measure expansion proved in Appendix A.3, combined with the fact that $r_\varepsilon(x) = 1 + \varepsilon(h(x) - \mathbb{E}_p[h]) + O(\varepsilon^2)$, which can be established using the same technique as in Appendix A.3. This yields

$$\mathbb{E}_p[g(X)(r_\varepsilon(X) - 1)] = \varepsilon \text{Cov}_p(g, h) + O(\varepsilon^2).$$

□

A.5. Score-model error decomposition and bound

Proposition A.6 (Fisher-controlled stability to score-model error). *Let p be the continuously differentiable training density on \mathbb{R}^d , let \tilde{p} be a learned density with score $\tilde{s} = \nabla \log \tilde{p}$, and let q be a test density such that $q \ll p$ with density ratio $l(x) = q(x)/p(x)$. Let $s_p = \nabla \log p$ and define*

$$g(x) := (\tilde{s}(x) - s_p(x))^\top \nabla f(x).$$

Assume $\tilde{s} - s_p \in L^2(p)$, $\nabla f \in L^4(p)$, and $l \in L^4(p)$. Then the score-model error term satisfies

$$|\langle g, l - 1 \rangle_{L^2(p)}| \leq \sqrt{J(p\|\tilde{p})} \|\nabla f\|_{L^4(p)} \|l - 1\|_{L^4(p)},$$

where

$$J(p\|\tilde{p}) := \mathbb{E}_p[\|\tilde{s}(X) - s_p(X)\|^2]$$

is the Fisher divergence of \tilde{p} from p .

Proof. By definition,

$$\langle g, l - 1 \rangle_{L^2(p)} = \mathbb{E}_p[(\tilde{s}(X) - s_p(X))^\top \nabla f(X) (l(X) - 1)].$$

Apply Cauchy–Schwarz in $L^2(p)$ by grouping the score-model error separately:

$$|\mathbb{E}_p[g(X)(l(X) - 1)]| \leq \left(\mathbb{E}_p[\|\tilde{s}(X) - s_p(X)\|^2]\right)^{1/2} \left(\mathbb{E}_p[\|\nabla f(X)\|^2(l(X) - 1)^2]\right)^{1/2}.$$

The first factor equals $\sqrt{J(p\|\tilde{p})}$ by definition. For the second factor, apply Hölder’s inequality with conjugate exponents 2 and 2:

$$\mathbb{E}_p[\|\nabla f(X)\|^2(l(X) - 1)^2] \leq (\mathbb{E}_p[\|\nabla f(X)\|^4])^{1/2} (\mathbb{E}_p|l(X) - 1|^4)^{1/2}.$$

Taking square roots of both sides gives

$$\left(\mathbb{E}_p[\|\nabla f(X)\|^2(l(X) - 1)^2]\right)^{1/2} \leq (\mathbb{E}_p[\|\nabla f(X)\|^4])^{1/4} (\mathbb{E}_p|l(X) - 1|^4)^{1/4} = \|\nabla f\|_{L^4(p)} \|l - 1\|_{L^4(p)}.$$

Combining the bounds yields

$$|\mathbb{E}_p[g(X)(l(X) - 1)]| \leq \sqrt{J(p\|\tilde{p})} \|\nabla f\|_{L^4(p)} \|l - 1\|_{L^4(p)},$$

as claimed. □

Remark. The same argument applies with any Hölder pair $p, q > 1$ satisfying $1/p + 1/q = 1$, yielding bounds involving higher-order $L^{2p}(p)$ and $L^{2q}(p)$ norms of ∇f and the density ratio $l - 1$, respectively.

B. Experimental setup and implementation details

This appendix provides implementation details for all experiments reported in Section 6, including model architectures, training procedures, score estimation, and evaluation protocols. All experiments are conducted in a fully *unsupervised* setting: neither the classifier nor the score model is trained or fine-tuned on any OOD data. We use Adam (Kingma & Ba, 2014) for all experiments.

B.1. Controlled 2D directional shift experiment

Data generation. Training samples are drawn from the standard 2-dimensional Gaussian $p(x) = \mathcal{N}(0, I_2)$. Test distributions are obtained by translating p by a fixed magnitude $\varepsilon = 10$ along directions $\varepsilon R_\varphi u$, where $u = (1, 1)^\top / \sqrt{2}$ and $\varphi \in [0, 2\pi)$. Each test set contains 1000 samples.

Model. The model is a fully connected ReLU network with a single hidden layer of size 64. The model is trained on samples from p using learning rate 0.001, for 100 epochs.

Stein quantities. Since p is known analytically, the score $s_p(x) = -x$ is used directly. Adjusted Stein residuals $r_f(x)$ are computed using Algorithm 1 and averaged across each test set to obtain an estimate of $S_f(p, q_\varphi)$.

B.2. MNIST geometric perturbation experiments

Dataset and preprocessing. MNIST images are zero-padded from 28×28 to 64×64 prior to training and evaluation. This padding ensures that translations do not remove semantic content, and it allows invariance effects to be isolated from boundary artefacts.

Perturbations. Test sets are generated using:

- Translations with ℓ^∞ magnitude $t \in \{0, 2, 4, \dots\}$. For each datapoint, the translation direction is chosen uniformly from a ℓ^∞ ball of desired radius.
- Rotations with angle $\alpha \in \{-90, -72, \dots, 72\}$ degrees.

Classifier. We use an AlexNet-style convolutional classifier adapted to single-channel inputs, with five 3×3 convolutional layers, ReLU activations, and channel widths 64, 192, 384, 256, and 256. Spatial downsampling is performed using average pooling, yielding feature maps of sizes 32×32 and 16×16 , followed by adaptive average pooling to a 1×1 resolution. The classifier head is a three-layer fully connected component with sizes $(512 \rightarrow 128 \rightarrow 10)$.

Score model. We use a lightweight convolutional score network to approximate the input-space score field $\hat{s}_p(x) \approx \nabla_x \log p(x)$. The model consists of four 3×3 convolutional layers with ReLU activations and channel widths 32, 64, 64, and 1, preserving the 64×64 spatial resolution throughout. The model is trained using Denosing Score Matching using standard practices.

Stein residuals. Adjusted Stein residuals $r_f(x)$ are computed using Algorithm 1, with the correction term D_f estimated on held-out MNIST training samples. The Laplacian was estimated using Hutchinson's estimator with the number of samples K set to 5.

B.3. CIFAR-10 benchmark evaluation

Classifier. The in-distribution classifier is a ResNet-18. We take model weights pre-trained on ImageNet and fine-tune it on CIFAR-10, with learning rate 0.0001 for 5 epochs.

Score model. The score function $\hat{s}_p(x)$ is estimated using a pretrained diffusion model. Specifically, we obtain the weights from the publicly released `google/ddpm-cifar10-32` checkpoint. The model is trained to predict the additive noise ε in the diffusion process, from which the score is obtained via the standard conversion $\hat{s}_p(x_t) = -\varepsilon_\theta(x_t, t) / \sigma_t$. While the diffusion model is trained over 1000 noise levels, we empirically find that evaluating the score at a relatively low time step ($t = 50$ out of 1000) yields a useful balance between proximity to the clean data score and numerical stability. Lower noise levels (smaller t) tend to produce noisier or unstable score estimates, whereas higher noise levels carry less information about the data distribution. Prior work on score-based models suggests that intermediate noise levels often provide the most

robust signal for downstream tasks (Song et al., 2021; Ho et al., 2020), even though they are not typically interpreted as clean-data scores per se. For empirical analysis see Appendix E.2.

B.4. Baselines and hyperparameters

All baseline methods are implemented using publicly available codebases or standard reference implementations (main dependency: pytorch-ood (Kirchheim et al., 2022)). Hyperparameters are selected according to the respective papers or using default setting provided in the package. Exact settings for MSP, ODIN, Mahalanobis, energy scores, kNN+, and GSC are summarised in below.

B.5. MVTec AD localisation experiments

Dataset. We use the MVTec Anomaly Detection dataset with the standard train/test split. Only `train/good` images are used for calibration.

Models.

- Classifier: ImageNet-pretrained ResNet-50, with weights downloaded thorough torchvision.
- Score model: ImageNet-pretrained diffusion model - obtained from the publicly available checkpoint HF checkpoint `google/ddpm-ema-celebahq-256`. Similarly to B.3, the score is obtained via the standard conversion $\hat{s}_p(x_t) = -\varepsilon_\theta(x_t, t)/\sigma_t$ with time step $t = 50$ (out of 1000).

No model is fine-tuned on MVTec AD.

Per-pixel Stein heatmaps. Per-pixel residuals are computed via the coordinate-wise Stein operator. Note that this gives a per-input score, and so there are three per pixel - one for each input channel. We take their sum to obtain the per-pixel score. Heatmaps are resized to 256×256 for inference and upsampled to ground-truth resolution for evaluation.

Evaluation. We report pixel-level AUROC, average precision, and AUPRO. Thresholds for visualisation are obtained via upper-tail calibration on `train/good` images at quantile $\alpha = 0.01$.

Additional qualitative results are shown in Appendix D.

C. Granular Experimental Results

Benchmark datasets and shift regimes. We evaluate task-aware OOD detection across a broad set of datasets designed to capture qualitatively different forms of distribution shift, ranging from semantic dataset shift to low-level corruptions, structured geometric perturbations, and adversarial examples, see also (Tajwar et al., 2021).

Classical OOD benchmarks. Following standard practice, we use SVHN, LSUN, iSUN, Describable Textures, and Places365 as semantic OOD datasets with respect to CIFAR-10. These datasets differ substantially from CIFAR-10 in terms of image content, statistics, and semantics, and are commonly used to benchmark the ability of OOD methods to detect inputs drawn from entirely different data-generating processes. SVHN consists of real-world digit images with markedly different backgrounds and color statistics; LSUN and iSUN contain large-scale scene images; Textures focuses on fine-grained texture patterns; and Places365 covers a wide range of scene categories. Together, these datasets probe classical semantic OOD detection, where the test distribution differs from the training distribution at a high semantic level.

CIFAR-10-C (common corruptions). To evaluate robustness under realistic covariate shift, we use CIFAR-10-C, which applies 19 common image corruptions—such as Gaussian noise, blur, fog, snow, contrast changes, and compression artifacts—each at five severity levels. These corruptions alter low-level image statistics while largely preserving high-level semantic content. CIFAR-10-C is widely used to assess distribution shift arising from sensor noise, environmental conditions, or data acquisition artifacts, and provides a systematic test of how OOD methods respond to gradual, non-adversarial changes in the input distribution.

CIFAR-10-P (structured perturbations). We additionally evaluate on CIFAR-10-P, which applies temporally consistent and structured geometric perturbations such as translations, rotations, scaling, shearing, and motion blur. Unlike CIFAR-10-C, these perturbations often leave pixel-level statistics relatively unchanged while inducing changes that directly interact with

the classifier’s invariances and equivariances. CIFAR-10-P therefore provides a particularly relevant testbed for *task-aware* OOD detection, as some perturbations (e.g. translations) are largely benign for convolutional networks, whereas others (e.g. rotations) can substantially degrade task performance despite minimal changes in overall image statistics.

Adversarial attacks. To probe behaviour under worst-case, task-adversarial distribution shifts, we include adversarial examples generated using FGSM, PGD, and AutoAttack under both ℓ^∞ and ℓ^2 constraints, with multiple perturbation budgets. These attacks are specifically constructed to induce classifier failure while keeping perturbations visually subtle and often imperceptible. Adversarial examples therefore represent a regime in which confidence-based and likelihood-based OOD methods are known to struggle, as inputs may remain close to the training distribution in pixel space while causing severe task-level errors. Including adversarial attacks allows us to assess whether task-aware Stein residuals respond to shifts that directly affect the predictor, even when traditional OOD signals fail.

Summary. Across these datasets, we cover four complementary shift regimes: (i) semantic dataset shift (classical OOD benchmarks), (ii) low-level covariate shift (CIFAR-10-C), (iii) structured, invariance-breaking perturbations (CIFAR-10-P), and (iv) worst-case, task-adversarial perturbations (adversarial attacks). This comprehensive evaluation enables a detailed assessment of how different OOD detection methods respond to shifts that are benign, harmful, or adversarial with respect to the underlying prediction task.

Granular results. Each table in this section reports a per-dataset breakdown for a single OOD detection method (see the baselines in Section 6.3 for details) and corresponds to one column of the aggregated results presented in the main text. AUROC is the area under the receiver-operator curve; FPR95 is the false positive rate at 95% true positive rate. These fine-grained results expose substantial variability in OOD detection performance across datasets, corruption types, and shift regimes. Such variability highlights the sensitivity of existing methods to the specific nature of distribution shift and provides additional empirical support for the central observation of Tajwar et al. (2021): namely, that no single OOD detection method consistently dominates across all benchmarks, and that comparative performance is strongly dataset-dependent.

Table 2. OOD detection results: adversarial

OOD Dataset	metric	MSP	Energy	ODIN	Mahalanobis	kNN+	GSC	TASTE (ours)
adversarial_autoattack_linf_2_255	AUROC	0.5019	0.4896	0.5393	0.5445	0.5276	0.5455	0.4786
	FPR95	0.9611	0.9643	0.93	0.9371	0.9513	0.8902	0.9571
adversarial_autoattack_linf_4_255	AUROC	0.2841	0.289	0.4851	0.505	0.3839	0.5277	0.6543
	FPR95	0.9681	0.9711	0.9532	0.9213	0.9711	0.9504	0.893
adversarial_autoattack_linf_8_255	AUROC	0.1557	0.1675	0.3319	0.7207	0.4341	0.6431	0.8609
	FPR95	0.9688	0.9713	0.9718	0.513	0.9688	0.9605	0.602
adversarial_fgsm_linf_4_255	AUROC	0.6254	0.6039	0.5673	0.6172	0.6266	0.6236	0.4866
	FPR95	0.923	0.9147	0.9306	0.9071	0.8999	0.8361	0.9508
adversarial_fgsm_linf_8_255	AUROC	0.6075	0.6026	0.5151	0.6341	0.6388	0.6051	0.4949
	FPR95	0.922	0.8993	0.9715	0.8969	0.8847	0.8524	0.948
adversarial_pgd_l2_0.5_steps=50	AUROC	0.2656	0.2741	0.5036	0.4714	0.3748	0.4665	0.5727
	FPR95	0.998	0.9985	0.9418	0.9507	0.9918	0.9745	0.9348
adversarial_pgd_l2_1.0_steps=50	AUROC	0.05975	0.07737	0.3817	0.634	0.311	0.5941	0.8612
	FPR95	1	1	0.9631	0.6251	0.9981	0.9984	0.5297
adversarial_pgd_linf_2_255_steps=50	AUROC	0.5837	0.5521	0.5402	0.5937	0.5812	0.5818	0.433
	FPR95	0.9646	0.9689	0.9205	0.9273	0.9484	0.8532	0.9637
adversarial_pgd_linf_4_255_steps=50	AUROC	0.3609	0.3548	0.5535	0.5159	0.4419	0.4719	0.5017
	FPR95	0.9908	0.9929	0.9151	0.9442	0.981	0.9442	0.9486
adversarial_pgd_linf_8_255_steps=50	AUROC	0.1304	0.1389	0.4769	0.5827	0.3248	0.5334	0.7578
	FPR95	0.9991	0.9997	0.9381	0.7652	0.996	0.9901	0.7966

TASTE: Task-Aware Stein OOD Detection

Table 3. OOD detection results: CIFAR-10-C

OOD Dataset	metric	MSP	Energy	ODIN	Mahalanobis	kNN+	GSC	TASTE (ours)
cifar10c_brightness	AUROC	0.5321	0.5389	0.4928	0.5356	0.543	0.5594	0.5373
	FPR95	0.9454	0.9354	0.9562	0.9452	0.939	0.8936	0.9335
cifar10c_contrast	AUROC	0.6945	0.7206	0.802	0.5841	0.6653	0.6424	0.6846
	FPR95	0.86	0.781	0.5962	0.929	0.8666	0.848	0.7849
cifar10c_defocus_blur	AUROC	0.5801	0.5763	0.5864	0.5667	0.5847	0.573	0.5842
	FPR95	0.9308	0.9212	0.8546	0.9318	0.9186	0.8724	0.8969
cifar10c_elastic_transform	AUROC	0.6027	0.6091	0.5777	0.5549	0.5956	0.5838	0.6088
	FPR95	0.9272	0.9236	0.8942	0.9504	0.9278	0.8726	0.8505
cifar10c_fog	AUROC	0.6217	0.6364	0.6875	0.5347	0.6108	0.6011	0.6465
	FPR95	0.9018	0.8914	0.7756	0.9596	0.9116	0.8474	0.8526
cifar10c_frost	AUROC	0.6086	0.6278	0.528	0.5703	0.6049	0.6094	0.627
	FPR95	0.9166	0.8964	0.957	0.9458	0.9148	0.8602	0.8693
cifar10c_gaussian_blur	AUROC	0.617	0.6142	0.6462	0.6018	0.6192	0.5965	0.6206
	FPR95	0.9222	0.9128	0.8006	0.9184	0.91	0.8576	0.8583
cifar10c_gaussian_noise	AUROC	0.6341	0.6509	0.4403	0.6333	0.646	0.6276	0.6332
	FPR95	0.8998	0.881	0.9884	0.8932	0.869	0.8476	0.8778
cifar10c_glass_blur	AUROC	0.6751	0.7104	0.5464	0.6415	0.6791	0.648	0.6725
	FPR95	0.882	0.8446	0.9454	0.8968	0.8704	0.8238	0.7801
cifar10c_impulse_noise	AUROC	0.702	0.7305	0.4776	0.7233	0.7255	0.6708	0.6812
	FPR95	0.865	0.8148	0.985	0.7908	0.7958	0.8264	0.7985
cifar10c_jpeg_compression	AUROC	0.5505	0.5577	0.5125	0.5168	0.5397	0.5603	0.5521
	FPR95	0.936	0.927	0.9338	0.9516	0.9344	0.8758	0.9042
cifar10c_motion_blur	AUROC	0.6302	0.6409	0.6239	0.6099	0.6453	0.6033	0.6365
	FPR95	0.9102	0.9062	0.8426	0.9094	0.8946	0.8512	0.8343
cifar10c_pixelate	AUROC	0.5407	0.5479	0.5094	0.5214	0.5376	0.5619	0.5486
	FPR95	0.9368	0.9178	0.9372	0.9408	0.9268	0.8882	0.9193
cifar10c_saturate	AUROC	0.5668	0.5892	0.5264	0.5833	0.5923	0.5875	0.5599
	FPR95	0.9298	0.9018	0.9292	0.9038	0.9024	0.8762	0.9253
cifar10c_shot_noise	AUROC	0.5986	0.6101	0.437	0.5952	0.6074	0.605	0.6015
	FPR95	0.9104	0.8944	0.9848	0.9096	0.8914	0.8536	0.9004
cifar10c_snow	AUROC	0.6104	0.6159	0.4865	0.5842	0.6032	0.6177	0.6169
	FPR95	0.9206	0.9046	0.972	0.9346	0.9134	0.8438	0.8872
cifar10c_spatter	AUROC	0.621	0.6448	0.4804	0.6007	0.626	0.6222	0.6176
	FPR95	0.905	0.8742	0.9726	0.9044	0.887	0.8506	0.892
cifar10c_speckle_noise	AUROC	0.6064	0.6209	0.444	0.6026	0.6138	0.6152	0.6119
	FPR95	0.9118	0.8902	0.9842	0.912	0.8878	0.8532	0.9009
cifar10c_zoom_blur	AUROC	0.6434	0.645	0.6435	0.6118	0.6466	0.6042	0.6444
	FPR95	0.895	0.8912	0.8146	0.9182	0.8952	0.8592	0.8275

TASTE: Task-Aware Stein OOD Detection

Table 4. OOD detection results: CIFAR-10-P

OOD Dataset	metric	MSP	Energy	ODIN	Mahalanobis	kNN+	GSC	TASTE (ours)
cifar10p_brightness	AUROC	0.5497	0.5549	0.499	0.5488	0.5583	0.5707	0.5557
	FPR95	0.9395	0.9357	0.9585	0.9415	0.934	0.8783	0.9205
cifar10p_gaussian_noise	AUROC	0.5069	0.5107	0.4618	0.4965	0.5076	0.5434	0.5107
	FPR95	0.9473	0.9454	0.9629	0.9559	0.9505	0.8995	0.9456
cifar10p_motion_blur	AUROC	0.6294	0.6368	0.6134	0.6183	0.6446	0.6063	0.6342
	FPR95	0.9197	0.9203	0.8495	0.9152	0.9095	0.8507	0.8123
cifar10p_rotate	AUROC	0.7012	0.7351	0.5982	0.6109	0.6842	0.6782	0.6822
	FPR95	0.8787	0.8463	0.9183	0.9477	0.8917	0.8101	0.731
cifar10p_scale	AUROC	0.6425	0.636	0.6375	0.6235	0.6482	0.6175	0.6448
	FPR95	0.9102	0.9122	0.8345	0.9203	0.9056	0.8348	0.8149
cifar10p_shear	AUROC	0.6641	0.6996	0.5723	0.5878	0.6514	0.6558	0.6496
	FPR95	0.8966	0.8619	0.921	0.938	0.8969	0.8365	0.8146
cifar10p_shot_noise	AUROC	0.5136	0.5184	0.4522	0.4989	0.5137	0.5458	0.5178
	FPR95	0.9444	0.9422	0.9708	0.9559	0.946	0.8938	0.9459
cifar10p_snow	AUROC	0.5989	0.6132	0.475	0.5697	0.5946	0.6123	0.6041
	FPR95	0.9179	0.905	0.9735	0.9357	0.9116	0.8551	0.8996
cifar10p_tilt	AUROC	0.5564	0.5699	0.5331	0.5059	0.5428	0.5538	0.5572
	FPR95	0.9378	0.9359	0.9293	0.9629	0.947	0.8846	0.8954
cifar10p_translate	AUROC	0.6523	0.6884	0.6304	0.5762	0.6388	0.6099	0.6318
	FPR95	0.9019	0.8788	0.9218	0.959	0.9148	0.8726	0.7862
cifar10p_zoom_blur	AUROC	0.5605	0.5583	0.5526	0.5457	0.567	0.5616	0.5676
	FPR95	0.9374	0.9411	0.9044	0.946	0.9379	0.883	0.8937

Table 5. OOD detection results: OOD benchmarks

OOD Dataset	metric	MSP	Energy	ODIN	Mahalanobis	kNN+	GSC	TASTE (ours)
iSUN	AUROC	0.7926	0.8561	0.682	0.8379	0.8203	0.7306	0.7408
	FPR95	0.7848	0.6455	0.9396	0.6829	0.6995	0.8223	0.5901
LSUN	AUROC	0.8208	0.8999	0.7047	0.88	0.8677	0.7636	0.7666
	FPR95	0.7391	0.5161	0.9421	0.5912	0.5945	0.8113	0.5364
Places365	AUROC	0.8005	0.854	0.7206	0.7943	0.8335	0.7715	0.7746
	FPR95	0.7878	0.6461	0.86	0.7714	0.6894	0.7432	0.5609
SVHN	AUROC	0.8044	0.816	0.9216	0.7705	0.8122	0.7106	0.749
	FPR95	0.8258	0.8118	0.4123	0.8402	0.7944	0.7934	0.5432
Textures	AUROC	0.7976	0.8339	0.7931	0.8113	0.8101	0.7384	0.7445
	FPR95	0.8018	0.7222	0.7239	0.7119	0.7358	0.7573	0.592

D. Per-pixel anomaly heatmaps

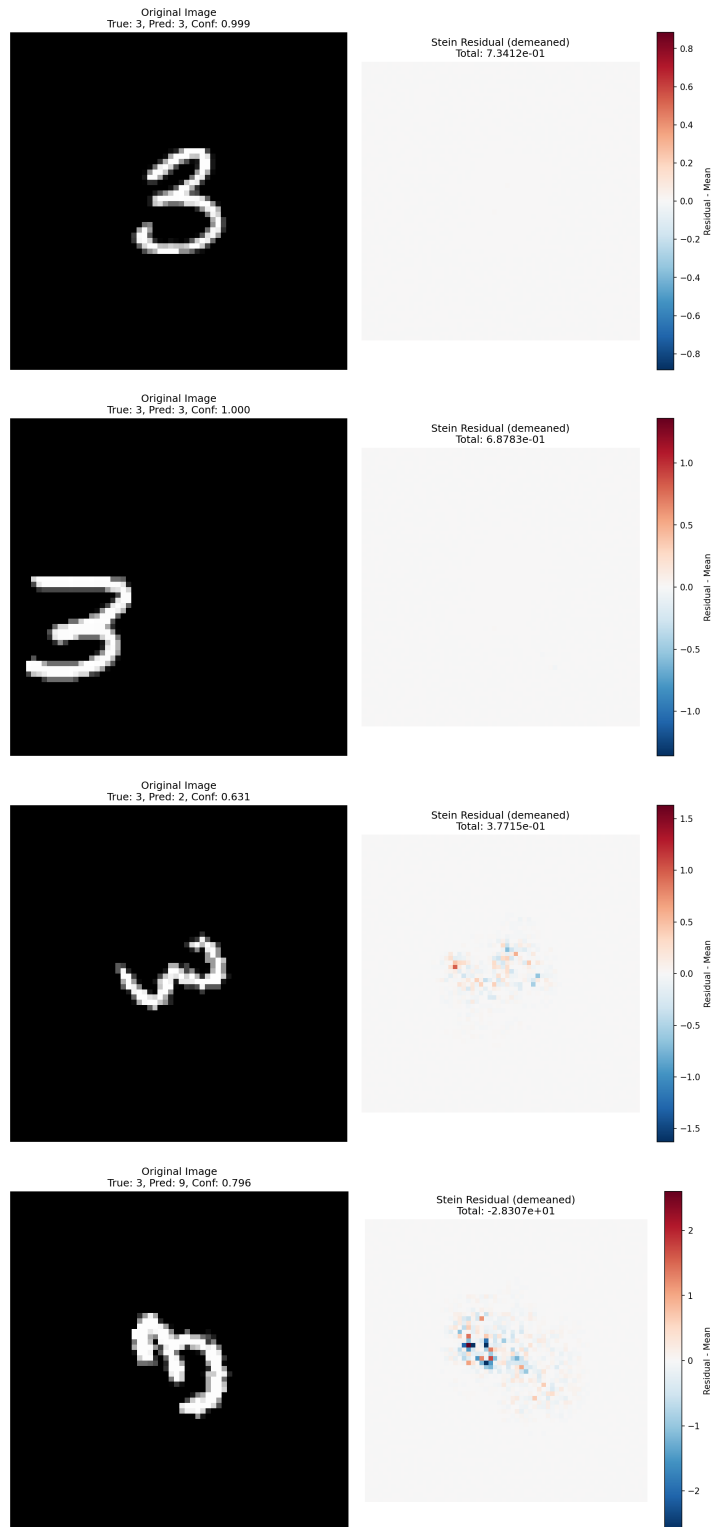


Figure 4. Demonstration of per-pixel anomaly heatmaps for the MNIST-based task. Input digits are shown on the left, while the heatmaps are on the right. Note that both original and translated digits do not generate significant anomaly signal.

TASTE: Task-Aware Stein OOD Detection

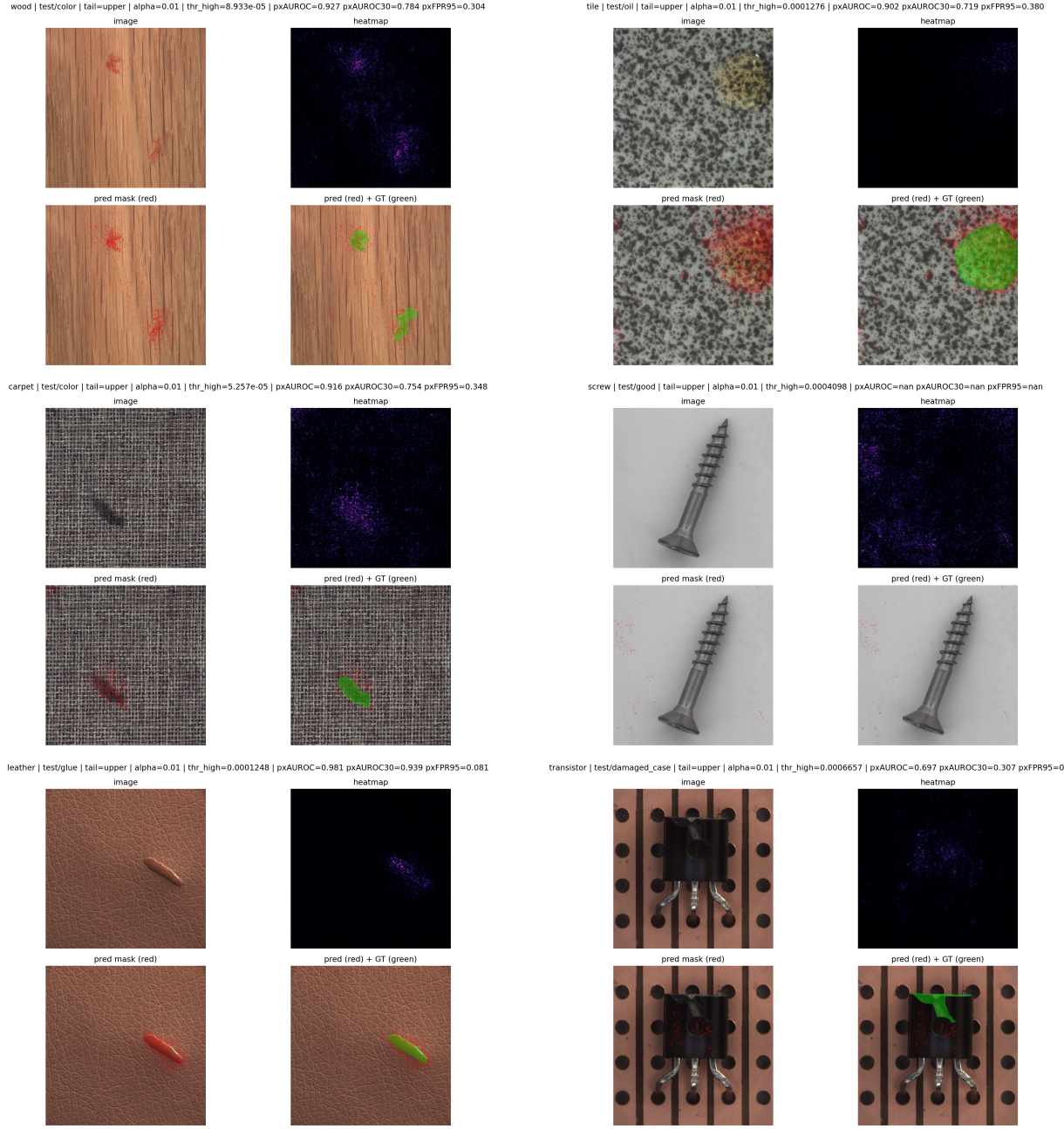


Figure 5. Additional qualitative results. Each panel is a randomly chosen example for one of MVtec AD categories. Within each panel there are four subplots: the original image (with corruption), detector’s heatmap, prediction overlay at $\alpha = 0.01$, prediction and ground truth (GT) overlay.

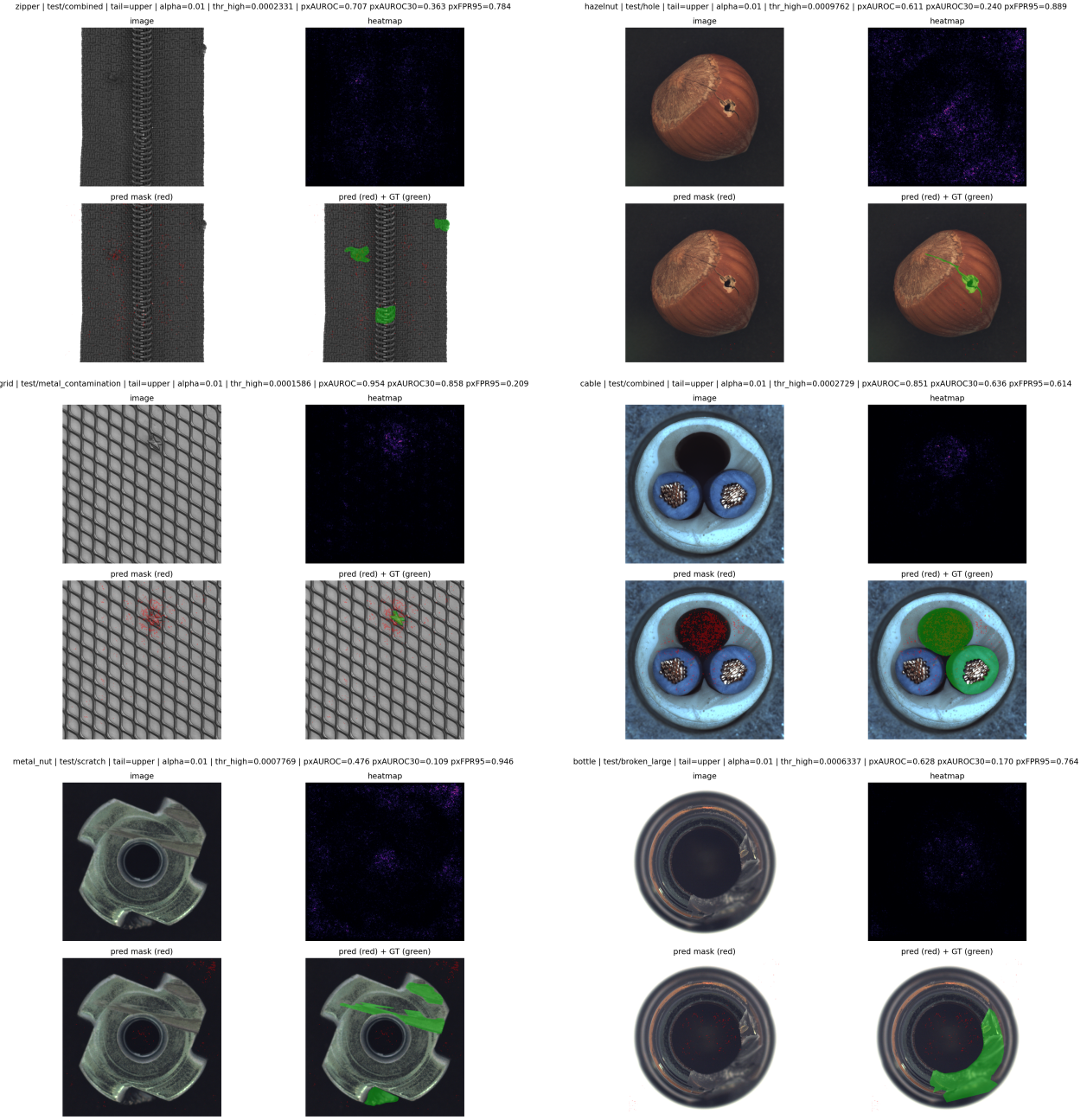


Figure 6. Additional qualitative results. Each panel is a randomly chosen example for one of MVTec AD categories. Within each panel there are four subplots: the original image (with corruption), detector’s heatmap, prediction overlay at $\alpha = 0.01$, prediction and ground truth (GT) overlay.

Observations. Figures 5 and 6 show that across MVTec AD categories, per-pixel Stein residuals can produce spatially coherent and visually meaningful localisation signals, particularly on texture classes, where defects manifest as systematic deviations in local appearance. Quantitative metrics and qualitative inspection indicate substantially weaker performance on object categories, where anomalies are often small, highly specific, and semantically defined (e.g. missing components or structural deformations). We hypothesise that such object-level defects are less accessible to a zero-shot pipeline based on a generic ImageNet-pretrained classifier and score model, which have not been exposed to object-specific normality constraints. Importantly, no component of our pipeline—neither the classifier nor the score model—has been trained or adapted on MVTec AD data, making this evaluation fully *zero-shot*.

Table 6. Operator construction ablation study - performance on CIFAR-10 across heterogeneous shift regimes. Results are averaged within each category. The dataset composition is identical to that used in the main evaluation suite presented in Section 6.3.

Method	Adversarial		CIFAR-10-C		CIFAR-10-P		OOD-benchmarks		Overall	
	AUROC↑	FPR95↓	AUROC↑	FPR95↓	AUROC↑	FPR95↓	AUROC↑	FPR95↓	AUROC↑	FPR95↓
TASTE	0.6144	0.865	0.6193	0.8691	0.5954	0.8611	0.7647	0.5677	0.6285	0.8263
TASTE-no-Laplacian	0.6264	0.8711	0.6098	0.8708	0.5902	0.8657	0.7597	0.5751	0.6253	0.8367
Score-only	0.5337	0.9437	0.6364	0.787	0.5789	0.8756	0.4452	0.8623	0.5783	0.8518

E. Ablation study

We present an ablation study designed to isolate the contribution of individual components of the Stein operator and sensitivity analysis to the choice of diffusion time step in the score model. The ablation (operator decomposition) is evaluated on the full CIFAR-10 OOD benchmark suite used in the main results, as it probes detection performance across heterogeneous shift regimes. The sensitivity analysis is done on a per-pixel level, using the MVTec AD dataset from the part of the paper.

E.1. Ablation: Operator decomposition

We study the effect of progressively simplifying the Langevin Stein operator by removing individual components. Specifically, we compare:

- **Full operator (TASTE):**

$$\mathcal{L}_p f(x) = \Delta f(x) + s_p(x)^\top \nabla f(x),$$

- **No-Laplacian:**

$$\mathcal{L}_p^{\text{no-lap}} f(x) = s_p(x)^\top \nabla f(x),$$

- **Score-only:** using only the score L^2 norm, without interaction with ∇f .

Table 6 reports performance across adversarial attacks, corruption benchmarks (CIFAR-10-C), structured perturbations (CIFAR-10-P), and standard OOD datasets. This setup is identical to experiments in Section 6.3.

Observations. Across all benchmark categories, the full operator and the no-Laplacian variant exhibit nearly identical performance, while the score-only variant performs substantially worse. In particular, the AUROC and FPR95 of TASTE and TASTE-NO-LAPLACIAN differ only marginally, whereas additionally removing the ∇f interaction leads to a pronounced drop in performance. This behaviour is explained by the dominance of the dot-product term $s(x)^\top \nabla f_c(x)$ in many practical settings. Specifically, the full score is dominated by

$$|s(x)^\top \nabla f_c(x)| \approx \|s(x)\| \|\nabla f_c(x)\| |\cos \theta_c|,$$

where θ_c is the angle between the score direction and the class-specific gradient. Empirically, we observe that while the gradient and the Laplacian are of comparable magnitude, the output of the score model is often much larger in scale, causing the dot-product term of the operator to dominate, even if the correlation between the score and the gradient is small.

Interpretation. From a computational perspective, Table 6 suggests that the Laplacian term can be omitted in many practical applications without significant loss in detection performance, yielding a cheaper first-order diagnostic. However, the theoretical guarantees developed in the main text rely on the full Langevin operator, and the Laplacian remains essential for ensuring a proper Stein identity and for avoiding directional blind spots in principle. We therefore view the Laplacian as theoretically fundamental but often numerically subdominant.

E.2. Sensitivity to diffusion time step

The per-pixel Stein residual depends on the quality and scale of the score estimate $\hat{s}_p(x) \approx \nabla_x \log p_t(x)$ produced by the diffusion model at a chosen time step t . Since the diffusion score interpolates between fine-grained data geometry (small t) and heavily smoothed distributions (large t), the time step implicitly controls the granularity of the resulting anomaly signal. We therefore study how per-pixel OOD performance varies as a function of t .

Setup. Using the MVTec AD dataset, we evaluate pixel-level anomaly detection metrics across a range of diffusion time steps while keeping all other components fixed: the classifier, Stein operator, residual aggregation, and evaluation protocol. For each time step, we compute per-pixel Stein heatmaps and report pixel-level AUROC, AUPRO, and average precision (AP), averaged across categories.

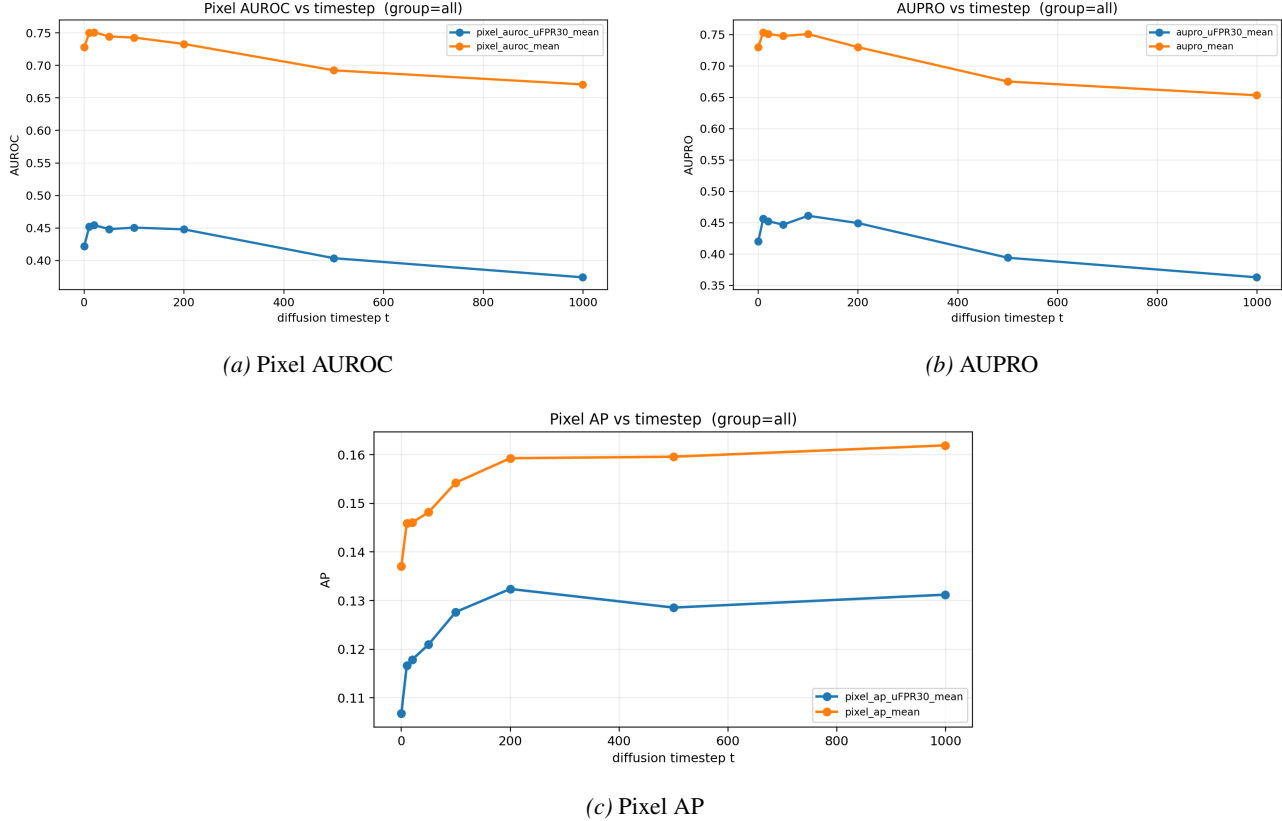


Figure 7. Effect of diffusion time step on per-pixel anomaly detection. As the diffusion time step increases, ranking-based metrics (AUROC, AUPRO) decrease, while average precision improves, indicating a shift from global separability to more confident, sparse anomaly responses. Metric in orange are standard area under curve statistics, while those in blue impose additional of False Positive Rate below 30% and thus promoting early separation.

Observed behaviour. Figure 7 shows a consistent and interpretable trade-off. As the diffusion time step increases, both pixel-level AUROC and AUPRO decrease, indicating reduced global separability and weaker region-level coherence of the anomaly scores. In contrast, average precision increases monotonically with time step. This divergence reflects a shift in the score distribution: higher time steps smoothen the score field and suppress moderate responses, while amplifying extreme deviations from the data manifold. As a result, fewer pixels receive large scores, but those that do are more likely to correspond to true defect regions.

Interpretation. These results highlight that different metrics probe distinct aspects of per-pixel anomaly detection. AUROC and AUPRO assess global ranking quality and spatial consistency, respectively, and therefore favour lower diffusion noise where fine-grained structure is preserved. Average precision, by contrast, emphasises the reliability of the highest-scoring pixels and is sensitive to the purity of the score tail. From this perspective, increasing the diffusion time step trades global separability for more confident, sparse anomaly responses. This behaviour is consistent with the geometry of diffusion score fields and suggests that the time step can be selected based on the desired operating regime: lower time steps for comprehensive localisation and higher time steps for high-confidence defect highlighting.

Practical Implications. This sensitivity analysis demonstrates that the proposed Stein residual does not behave arbitrarily with respect to the score model, but exhibits predictable and structured changes as the underlying notion of data geometry is varied. In all cases, the method remains fully zero-shot, requiring no retraining or fine-tuning on the target dataset.

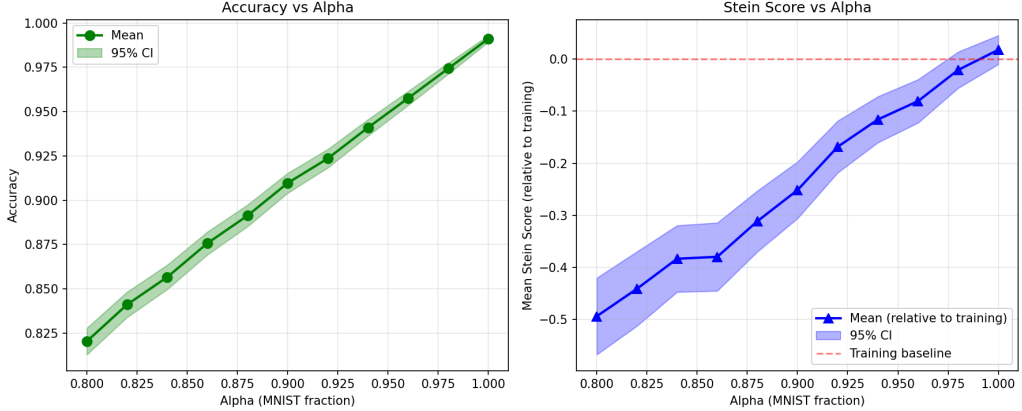


Figure 8. Model performance and Stein signal as a function of test set corruption level. The methodology picks up on the presence of out-of-distribution input data for even very small corruption levels.

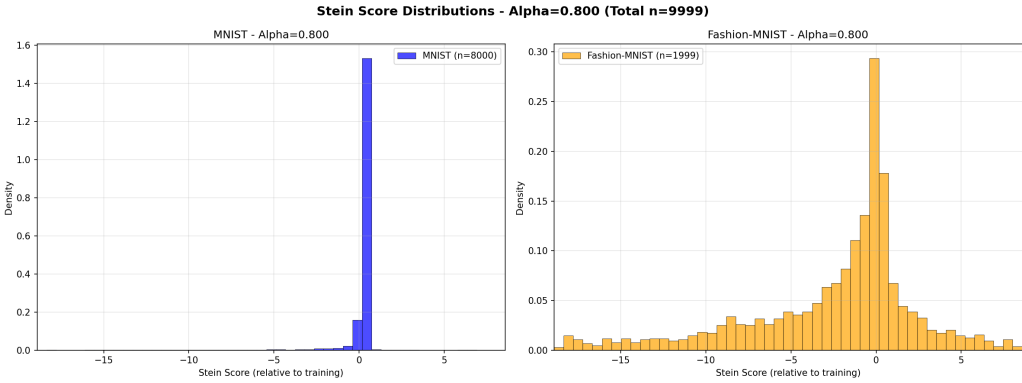


Figure 9. Distribution of the per-sample Stein score. The left panel shows evaluation on clean (MNIST) samples, while the right presents the scores generated from corrupted data. The considerable distribution shift of the per-sample Stein score allows for per-input anomaly detection.

F. Per-sample Stein residuals in mixed MNIST / Fashion-MNIST OOD

We now assess the discriminative power of *per-sample* Stein residuals in a heterogeneous OOD scenario based on mixed in- and out-of-distribution test sets, a setting that is known to be challenging for OOD detection and has been used to expose failure modes of likelihood-based and confidence-based approaches (Nalisnick et al., 2019; Rabanser et al., 2019).

Setup. The classifier f_θ and score model \hat{s}_p are trained exactly as in the previous subsection. Test sets are constructed by mixing MNIST (in-distribution) and Fashion-MNIST (OOD) according to a corruption level $\beta \in \{0.80, 0.82, \dots, 1.00\}$, where the test set contains $\beta \cdot 10,000$ MNIST images and $(1 - \beta) \cdot 10,000$ Fashion-MNIST images.

Aggregate behaviour. For each α we compute the classifier accuracy and the mean Stein signal. As shown in Figure 8, both quantities vary monotonically with the corruption level: accuracy declines as Fashion-MNIST content increases, while the Stein score increases in magnitude.

Per-sample separation. For a fixed corruption level (e.g. $\beta = 0.8$), the distribution of $r_f(x)$ is sharply concentrated near zero for MNIST and displays heavy tails for Fashion-MNIST (Figure 9). This separation enables a simple calibrated test: using held-out MNIST data, estimate the 95th percentile $\tau_{0.95}$ of $|r_f(x)|$ and declare a test point OOD if $|r_f(x)| > \tau_{0.95}$. The resulting test achieves high power across all corruption levels (Figure 10) despite requiring no supervision on Fashion-MNIST.

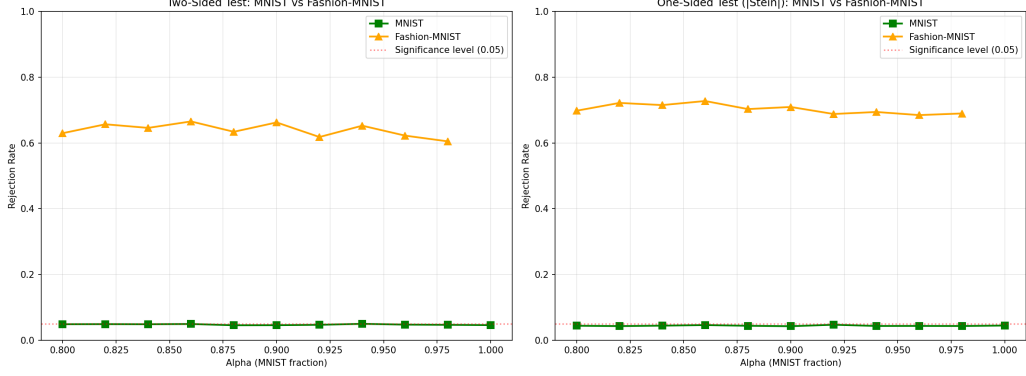


Figure 10. Stein score-based test power comparison as a function of test set corruption level α . The left panel presents results for two-sided tests, while one-sided (arguably more powerful) test is presented on the right. Also, see Appendix C for power analysis based on a first-order operator

G. First-Order Stein Operator Diagnostics

For a function $f \in \mathcal{F}(p)$, instead of the Langevin operator $\mathcal{L}_p f(x) = \Delta f(x) + \nabla \log p(x)^\top \nabla f(x) \in \mathbb{R}$, consider a first-order Stein operator defined as

$$\mathcal{A}_p f(x) = \nabla f(x) + f(x) s_p(x) \in \mathbb{R}^d.$$

To obtain a scalar diagnostic one typically projects this vector onto a fixed direction v , which we denote by

$$\mathcal{A}_p^v f(X) = v^\top \nabla f(x) + f(x) v^\top s_p(x) \quad (20)$$

It is easy to show that $\mathbb{E}_p[\mathcal{A}_p^v f(X)] = 0$ under mild assumptions on f . Indeed, let $X \sim p$ and assume $f \in \mathcal{F}(p)$ is such that the following integration by parts is valid (e.g., $f p$ vanishes at infinity). Then

$$\mathbb{E}_p[\mathcal{A}_p^v f(X)] = \mathbb{E}_p[v^\top \nabla f(X)] + \mathbb{E}_p[f(X) v^\top s_p(X)]. \quad (21)$$

Since $s_p = \nabla \log p$, we have $f s_p = \nabla(f p)/p - \nabla f$, and thus

$$\mathbb{E}_p[f(X) v^\top s_p(X)] = \int v^\top f(x) \nabla \log p(x) p(x) dx = \int v^\top \nabla(f(x)p(x)) dx - \int v^\top \nabla f(x) p(x) dx.$$

Under the assumed boundary conditions, the first integral vanishes, yielding

$$\mathbb{E}_p[f(X) v^\top s_p(X)] = -\mathbb{E}_p[v^\top \nabla f(X)].$$

Substituting back into (21), the two terms cancel and we obtain

$$\mathbb{E}_p[\mathcal{A}_p^v f(X)] = 0.$$

We now consider q , another smooth density on \mathbb{R}^d , absolutely continuous with respect to p . Mirroring the argument from the main text, we obtain

$$\mathbb{E}_q[\mathcal{A}_p^v f(X)] = -v^\top \mathbb{E}_q \left[f(X) \nabla \log \frac{q(X)}{p(X)} \right].$$

Indeed, taking expectation under q yields

$$\mathbb{E}_q[\mathcal{A}_p^v f(X)] = v^\top \mathbb{E}_q[\nabla f(X)] + v^\top \mathbb{E}_q[f(X) \nabla \log p(X)].$$

Using integration by parts under q and the identity

$$\mathbb{E}_q[\nabla f(X)] = -\mathbb{E}_q[f(X) \nabla \log q(X)],$$

which holds for f in the Stein class, we obtain

$$\mathbb{E}_q[\mathcal{A}_p^v f(X)] = -v^\top \mathbb{E}_q[f(X)(\nabla \log q(X) - \nabla \log p(X))].$$

Rearranging terms gives

$$\mathbb{E}_q[\mathcal{A}_p^v f(X)] = -v^\top \mathbb{E}_q\left[f(X)\nabla \log \frac{q(X)}{p(X)}\right],$$

as claimed.

Thus this functional detects only *value-based alignment*: between the output $f(X)$ and the score mismatch $\nabla \log(q/p)(X)$. In contrast to the Langevin operator, which probes geometric distortions via $\nabla f(X)$ and $\Delta f(X)$, the first-order functional reacts primarily to changes in the distribution of the scalar outputs $f(X)$. This might lead to unexpected behaviour.

G.1. Directional blind spots: the 2D Gaussian illustration

To illustrate the potential blind spots, consider the two-dimensional Gaussian mean-shift model introduced in Section 6.1 of the main text

$$p(x) = \mathcal{N}(0, I_2), \quad q(x) = \mathcal{N}(\varepsilon u, I_2), \quad u = (\cos \theta, \sin \theta).$$

For the task $f(x) = x_2 - x_1$, the scalar first-order functional admits the exact expression

$$\mathbb{E}_q[\mathcal{A}_p^v f(X)] = -\varepsilon^2 (v_1 \cos \theta + v_2 \sin \theta) (\sin \theta - \cos \theta).$$

For $v = (1, 1)$ this expression simplifies to

$$\mathbb{E}_q[\mathcal{A}_p^v f(X)] = \varepsilon^2 \cos(2\theta)$$

which corresponds to taking the component-wise average of the operator.

Thus the response is *quadratic* in the shift magnitude and vanishes for all $\theta = \pi/4, 3\pi/4, \dots$, creating entire undetectable families of distributional shifts (see Figure 11). By contrast, the Langevin Stein operator responds linearly in ε and exhibits no such degeneracies.

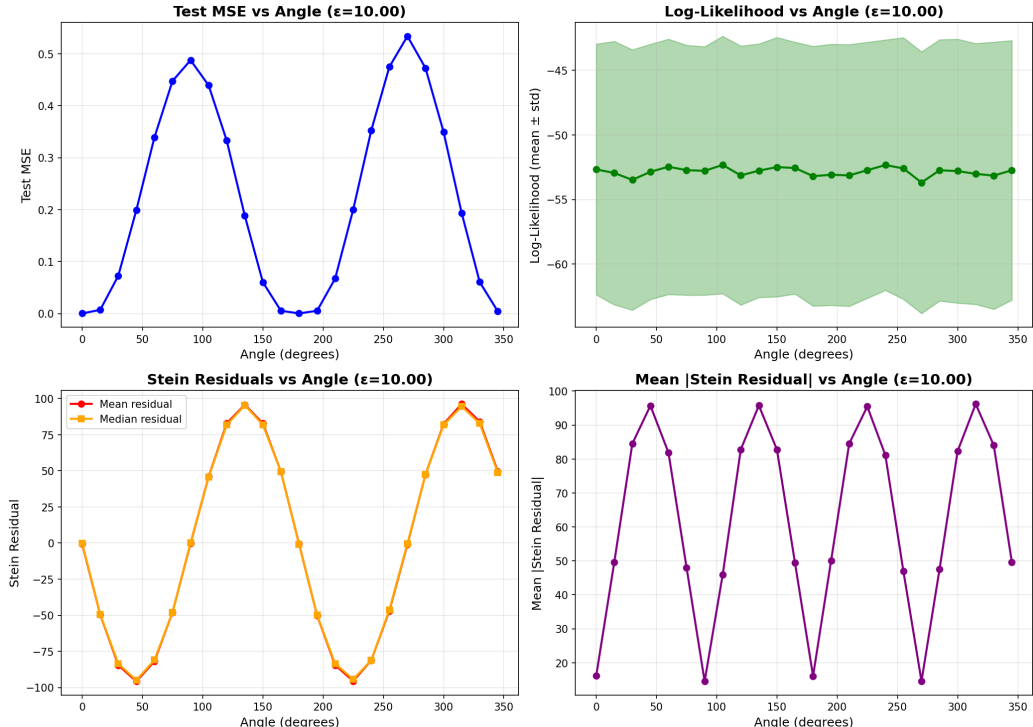


Figure 11. Directional evaluation of model sensitivity and OOD scoring under the first-order Stein operator (20). This figure should be compared with Figure 2. The signal generated by the (analog of the) TASTE functional for the first-order Stein operator no longer aligns with performance.

G.2. The L^2 norm of the first-order Stein operator (no blind spots, but not a Stein operator)

Another way to obtain a scalar quantity - and perhaps more natural - is to consider the squared L^2 norm of the operator, test distribution q :

$$\mathcal{T}_f(p, q) := \mathbb{E}_q \left[\left\| \mathcal{A}_p f(X) \right\|_2^2 \right] = \mathbb{E}_q \left[\left\| \nabla f(X) + f(X) s_p(X) \right\|_2^2 \right]. \quad (22)$$

No blind spots. Unlike the linear functional $\mathbb{E}_q[\mathcal{A}_p^v f]$, which can vanish for large families of shifts (e.g. whole cones of directions in the 2D Gaussian example), the quadratic quantity (22) is much harder to drive to zero. Thus the L^2 norm of the full first-order field does not suffer from the same directional “blind spot” issues as the projected linear functional.

Nonlinearity and the loss of the Stein property. A key drawback is that $\|\mathcal{A}_p f\|_2^2$ is *not* linear in f or in the operator. Therefore,

$$\mathbb{E}_p \left[\left\| \mathcal{A}_p f(X) \right\|_2^2 \right] \neq 0$$

in general. In fact, for any nontrivial f in the Stein class of p ,

$$\mathbb{E}_p \left[\left\| \mathcal{A}_p f(X) \right\|_2^2 \right] = \text{Var}_p(\mathcal{A}_p f(X)) > 0.$$

Thus $\mathcal{T}_f(p, q)$ is *not* a Stein operator: it does not vanish under the null hypothesis that $q = p$ and therefore cannot be used directly for discrepancy testing. To convert it into a usable shift-sensitive statistic, we apply the same principle used for correcting misspecified score models: subtract the empirical baseline under the training distribution. Under $q = p$, this corrected statistic concentrates near zero, although this is more of a heuristic and does not have the same theoretical properties as a proper Stein operator. Under $q \neq p$, we see that it typically becomes positive because the magnitude of the first-order field changes whenever the distributional shift interacts with either f or s_p .

Informally, unlike the linear first-order TASTE functional, the squared-norm statistic captures *both magnitude and directional* changes in $\nabla f + f s_p$, thus eliminating blind spots.